Charles University

Faculty of Science

Study programme: Chemistry

Branch of study: NBIOFYZD

Bc. Jakub Čopák

Quantum optical nanosensors for microRNA Supervisor:

Nanosenzory pro kvantově-optickou detekci mikroRNA

Diploma thesis

Supervisor: Mgr. Petr Cígler, Ph.D.

Prague, 2021

Prohlášení:

Prohlašuji, že jsem závěrečnou práci zpracoval samostatně a že jsem uvedl všechny použité informační zdroje a literaturu. Tato práce ani její podstatná část nebyla předložena k získání jiného nebo stejného akademického titulu.

V Praze, dne . . . . . Podpis . . . . . .

Acknowledgements

In the first place, I would like to thank to my girlfriend Týna. For the incredible motivation to write my diploma thesis as soon as possible, for the encouraging words, for all the support in the recent months and for a thorough language check of my work.

It's a great pleasure to thank to my supervisor Petr Cígler, for leading my diploma thesis. For his friendly approach, encouraging and especially highly professional advice, his unceasing enthusiasm for research and for the long days of commenting on the texts for my diploma thesis.

Furthermore, I would like to thank all the people from our lab for creating a perfect working atmosphere. I am particularly grateful for proofreading of my thesis by Michal Gulka. My sincere acknowledgments also belong to Chandra Epperla for his professional advice in experimental work as well as in the writing. Especially, I would like to thank Jiří Schimer for help with the organic part of the synthesis.

Finally, I would like to thank Priya Balasubramanian and Maabur Sow from the Ulm University for measuring the T_1 relaxation times.

Special thanks to my family for all the support throughout my life.

Abstract

Several disease processes taking place in the cells are characterized by an increase of the concentration of nucleic acids, in particular micro RNAs (miRNAs). A detection system that could selectively detect the increased presence of the miRNAs directly in the living cells in real time with nanoresolution is therefore highly desired. Fluorescent nanodiamond particles are considered promising candidates thanks to their biocompatibility, small size, allowing them to penetrate the cell membrane, and stable fluorescent defects in the crystal lattice, namely nitrogen-vacancy (NV) centres. The NV centres are the most studied colour centres of nanodiamonds due to their unique room-temperature optical properties, allowing for highly sensitive detection of changes in the magnetic field (magnetic noise) with quantum sensing techniques. For instance, the length of the T_1 relaxation time NV electronic spin is greatly influenced by the presence of paramagnetic species, which causes a shortening of the T_1 relaxation time depending on the proximity to the NV centres. However, for selective quantum sensing with nanodiamonds, the use of molecular transducers is necessary to bind targeted molecules with high specificity and allow their detection via the change of the NV spin properties. In this work, miRNAs-selective probes are developed based on the fluorescent nanodiamonds with covalently attached molecular beacons on their surface as a transducer. The sensing mechanism is based on gadolinium paramagnetic ions (Gd^{3+}), which are attached to the end of the molecular beacons and generate significant magnetic noise (thus shortening the T_1 relaxation time). After binding the target miRNA molecule, molecular beacons open up and the Gd^{3+} ions are moved further from the fluorescent nanodiamonds. Successful detection of the miRNA molecules is monitored optically by a prolongation of the T_1 relaxation time of the NV centres. This work represents a first step for localized and selective detection of miRNA, which would enable to identify disease processes inside living cells at an early stage.

Keywords: nanodiamonds, NV centres, molecular beacons, T_1 relaxation time, gadolinium, quantum sensing, fluorescence

Abstrakt

Patologické procesy probíhající v buňkách jsou v mnohých případech charakterizovány zvýšením koncentrace nukleových kyselin zvaných mikro RNA (miRNA). Detekční systém, který by dokázal v reálném čase a s nanorozlišením selektivně detekovat zvýšenou přítomnost miRNA přímo v živých buňkách, je proto velmi žádoucí. Slibným kandidátem jsou fluorescenční nanodiamantové částice, které jsou biokompatibilní, mají malé rozměry umožňující proniknout do buněčné membrány a obsahují stabilní fluorescenční defekty v krystalové mřížce, konkrétně centra dusík-vakance (NV). NV centra jsou díky svým jedinečným optickým vlastnostem nejstudovanějšími barevnými centry v nanodiamantech. Pomocí kvantových detekčních technik jimi lze při pokojové teplotě detekovat s vysokou citlivostí změny v magnetickém poli (magnetický šum). Například délka T_1 relaxačního času elektronového spinu NV centra je silně ovlivněna přítomností paramagnetických částic, které T_1 čas zkracují, a to v závislosti na jejich vzdálenosti od NV center. Pro selektivní kvantovou detekci pomocí nanodiamantů je však nezbytné použití chemických převodníků, které slouží k navázání detekovaných molekul s vysokou specificitou a zároveň umožnují jejich následnou detekci ovlivněním spinových vlastností NV center. V této práci jsou vyvinuty selektivní sondy z fluorescenčních nanodiamantů, na které jsou kovalentně navázány „molekulární majáčky“ (molecular beacons) plnící funkci takovéhoto chemického převodníku. Detekční mechanismus je založený na paramagnetických iontech gadolinia (Gd^{3+}), které jsou připojeny k jednomu konci molekulárních majáčků a generují silný magnetický šum (čímž zkracují T_1 relaxační čas). Po navázání cílové molekuly miRNA se molekulární majáčky otevřou a přemístí tak ionty Gd^{3+} dále od nanodiamantů. Úspěšná detekce molekul miRNA je monitorována opticky prodloužením T_1 relaxačního času NV center. Tato práce je prvním krokem pro lokalizovanou a selektivní detekci miRNA, což by umožnilo identifikovat chorobné procesy uvnitř živých buněk v jejich rané fázi.

Klíčová slova: nanodiamanty, NV centra, molekulární majáčky, T_1 relaxační čas, gadolinium, kvantové snímaní, fluorescence

List of abbreviations

- **ACN** acetonitrile
- **AT** adenine and thymine
- **BHQ-1** Black Hole Quenchers 1
- **BHQ-2** Black Hole Quenchers 2
- **cDNA** complementary deoxyribonucleic acid
- **CVD** chemical vapour deposition
- **Dabcyl** 4-(dimethylaminoazo)benzene-4-carboxylicacid
- **DBCO** dibenzocyclooctyne
- **DGCR8** DiGeorge syndrome critical region 8
- **DMSO** dimethyl sulfoxide
- **DNA** deoxyribonucleic acid
- **DNDs** detonation nanodiamonds
- **EPR** electron paramagnetic resonance
- **ESI** electrospray ionization
- **FNDs** fluorescence nanodiamonds
- **GC** guanine and cytosine
- **HEPES** 4-(2-hydroxyethyl)-1-piperazineethanesulfonic acid
- **HOXD10** homeobox D10
- **HPHT** high pressure, high temperature
- **HPLC** high-performance liquid chromatography
- **ICP-MS/MS** inductively coupled plasma – mass spectrometry
- **LC-MS** liquid chromatography coupled with a mass detector
- **LNAs** locked nucleic acids
- **MB** molecular beacon
- **mRNA** messenger ribonucleic acid
- **miRNA** micro ribonucleic acid
- **NBS** *N*-bromosuccidimide
- **NDs** nanodiamonds
- **NHS** *N*-hydroxysuccinimide
- **NIPAM** *N*-isopropylacrylamide

- **NV** nitrogen-vacancy
- **ODMR** optically detected magnetic resonance
- **PBS** phosphate-buffered saline
- **PCR** polymerase chain reaction
- **PEG** poly(ethylene glycol)
- **PDCD4** programmed cell death protein 4
- **PTEN** phosphatase and tensin homolog
- **QPCR** quantitative polymerase chain reaction
- **RISC** ribosomal ribonucleic acid-induced silencing complex
- **RNAP II** ribonucleic acid polymerase II
- **rRNA** ribosomal ribonucleic acid
- **RT** room temperature
- **SBR** signal-to-background ratio
- **SNPs** single-nucleotide polymorphisms
- **T_m** melting temperature
- **TNT** trinitrotoluene
- **TOF** time of flight
- **tRNA** transfer ribonucleic acid
- **TsN_3** tosylazide
- **USSR** Union of Soviet Socialist Republics
- **ZPL** zero phonon line

Contents

1. Introduction

A lot of attention is being paid to the development of new drugs, however, the advancement of new diagnostic methods should certainly not be forgotten. It is the early detection of disease processes at the cellular level that can lead to a breakthrough in the diagnosis of various diseases, such as cancer. For instance, changes in cellular metabolism are signalled by a change in the concentration of small RNA molecules – microRNA (miRNA) molecules.

The methods used so far to detect miRNAs are quite sensitive but their biggest disadvantage lays in the impossibility of using these techniques directly in the living cells. It is therefore desired to develop a method that could eliminate such a shortcoming.

One of the ways to detect miRNA molecules at very low concentrations and with high selectivity is to use molecular beacons. In this work, we focused on the design and preparation of a detection system based on a combination of molecular beacons and luminescent nanodiamonds. This combination allows optical detection of miRNAs based on the quantum sensing techniques employing nitrogen-vacancy (NV) defects in the diamond lattice. The binding of the miRNA molecule to the molecular beacons on the nanodiamonds surface is monitored by the shortening of NV electronic spin relaxation time.

2. Theoretical part

2.1 MicroRNAs

The discovery of microRNAs (miRNAs) is relatively recent. It is less than 30 years since Victor Amros'[1] and Gary Ruvkun's[2] groups discovered protein regulation, governed by a small molecule of RNA. That was in 1993. About seven years later, another small RNA molecule – *let-7*, was identified in several species.[3,4] This discovery was groundbreaking and since then, the number of published papers dealing with miRNAs has been growing year by year. MiRNAs have been found so far in various organisms such as viruses, green algae, plants or more deeply branching animals.[5]

MiRNAs are small RNA molecules usually composed of 22 nucleotides. Besides length and function, they do not differ broadly from well-known RNA molecules (mRNA, rRNA or tRNA). MiRNAs are noncoding RNA molecules whose main role is gene expression regulation. Some types of miRNAs are characteristic for a certain type of tissue. For example, high concentration of *miR-122* was found in liver, whereas *miR-124* was found mainly in neurological tissues.[6,7] However, some miRNAs molecules that are commonly present in cells and tissues can be also found in extracellular fluids such as plasma, serum, urine or saliva (for more information see *Table 2.1*).

Table 2.1: The top twenty most abundant miRNAs in selected extracellular fluids, from top to bottom according to decreasing concentration. MiRNAs, which occur in only one fluid in this table, are highlight in red. Table adopted from.[8]

Plasma	Tears	Urine	Breast milk	Seminal fluid	Saliva	Colostrum
miR-335*	miR-335*	miR-515-3p	miR-335*	miR-518e	miR-335*	miR-509-5p
miR-325	miR-515-3p	miR-335*	miR-26a-2*	miR-590-3p	miR-892a	miR-181d
miR-377*	miR-137	miR-892a	miR-181d	miR-588	miR-515-3p	miR-335*
miR-586	miR-509-5p	miR-509-5p	miR-509-5p	miR-873	miR-545*	miR-518e
miR-518e	miR-590-3p	miR-223*	miR-524-5p	miR-590-5p	miR-27a	miR-515-5p
let-7i	miR-873	miR-873	miR-137	miR-197	miR-518e	miR-223*
miR-539	miR-892a	miR-302d	miR-26a-1*	miR-218	miR-509-5p	miR-671-5p
miR-616*	miR-223*	miR-616*	miR-595	miR-515-5p	miR-492	miR-873
miR-302d	miR-302d	miR-134	miR-580	miR-137	miR-483-5p	miR-483-5p
miR-589	miR-590-5p	miR-923	miR-130a	miR-335*	miR-923	miR-186
miR-556-3p	miR-195	miR-483-5p	miR-515-3p	miR-617	miR-873	miR-515-3p
miR-151-3p	miR-130a	miR-101*	miR-513c	miR-410	miR-92b	miR-616*
miR-548b-3p	miR-675	miR-325	miR-671-5p	miR-524-5p	miR-302d	miR-134
miR-192	miR-29b	miR-589	miR-490-5p	miR-20b	let-7a	miR-892a
miR-151-5p	miR-616*	miR-556-3p	miR-367	miR-181d	miR-580	miR-590-5p
miR-598	miR-410	miR-545*	miR-181b	miR-1	miR-616*	miR-590-3p
miR-187	miR-101*	miR-377*	miR-598	miR-671-5p	miR-134	miR-425
miR-873	miR-134	let-7i	miR-515-5p	miR-509-5p	miR-25*	miR-454
miR-218	miR-487b	miR-890	miR-578	miR-515-3p	let-7i	miR-101*
miR-923	miR-483-5p	miR-505	miR-487b	miR-892a	miR-410	miR-132

Their increased or decreased concentration in certain cell types usually indicates disease-related processes, such as those associated with cancer, cardiac or immunity-related disease.[9] Therefore, the presence of some types of miRNAs in body fluids at various concentrations can be used as a biomarker for the early detection of cancer or other diseases, which can represent a significant progress in the treatment. Almost every type of cancer is characterized by a specific

profile of upregulated and downregulated miRNAs compared to normal cells from the same tissue.[9] Recognition of such profile for each tumour could significantly advance cancer diagnosis and treatment and therefore the study of miRNAs as cancer biomarkers has a high potential.

For instance, members of the *let-7* miRNA family that inhibit cancer growth are downregulated in multiple malignancies.[10] In a study of 143 patients with lung cancer, patients with reduced *let-7* expression had a significantly lower survival after resection.[11] Another well-researched example is *miR-21*, which is upregulated in several types of solid tumours as well as in hematologic malignancies and plays role in the regulation of tumour-suppressor genes such as PTEN[12] and PDCD4.[13] In a study of 84 patients with colon adenocarcinoma, increased *miR-21* expression was associated with lower survival.[14] Another example is *miR-10b*, which has been implicated in the suppression of HOXD10, thereby promoting metastasis.[15]

The computer approach for the miRNA molecules identification lies in the search for evolutionarily conserved sequences.[16] Up to now, more than 2 000 human miRNAs have been identified and this number is expected to continue to increase.[17]

2.1.1 MiRNA synthesis in the cells

The synthesis of miRNA begins in the cell nucleus similarly to the well-known RNA molecule – mRNA. The pri-miRNA transcription from the appropriate gene is carried out by RNA polymerase II (RNAP II) or RNA polymerase III enzymes. The resulting pri-miRNA is composed of a loop, a double strand (not completely complementary) and two single strands (see *Figure 2.1*). The pri-miRNA single strands are cleaved immediately after transcription by Drosha endonuclease, resulting in an approximately 70-nucleotides-long step-loop structure called pre-miRNA. It should be noted that Drosha is a part of a larger microprocessor complex and double-stranded RNA binding protein DGCR8 (called Pasha) is required for Drosha to function properly.[18] Pre-miRNA is then transported by exportin-5 from the nucleus to the cytosol. Subsequently, in the cytosol, endonuclease called Dicer cleaves the miRNA, creating a miRNA-miRNA*.[19] In the last step, this duplex is disintegrated and miRNA* is degraded. MiRNA, however, is bound to the RNA-induced silencing complex (RISC), which preserves miRNA against degradation.[20]

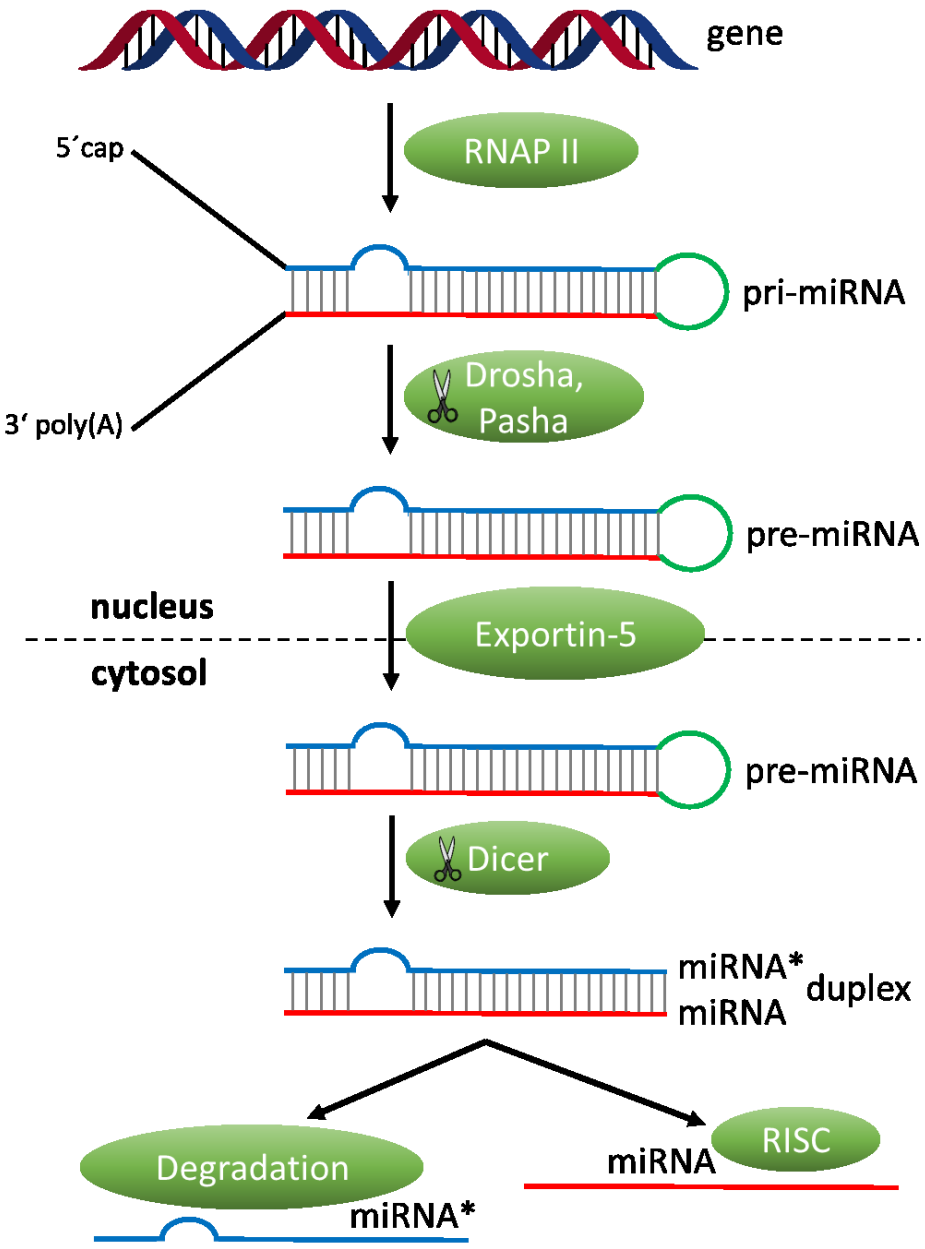

Figure 2.1: Scheme of miRNA synthesis

2.1.2 MiRNA regulation

The role of miRNA is to regulate mRNA translation and degradation. The mechanism of this regulation depends on how complementary the miRNA is to the corresponding mRNA molecule. The miRNAs that are completely or almost completely complementary to mRNA regulate degradation by the RISC, while miRNA molecules with low compatibility block the translation of mRNA on the ribosome.[21]

However, identifying a target molecule for a given miRNA is very difficult because of the 22 nucleotides, which make up the miRNA, only 6 – 8 nucleotides match perfectly with the target

mRNA's 3' untranslated region.[22] These nucleotides are called seed sequence. The remaining nucleotides of the miRNA sequence may bind perfectly or even minimally to the target mRNA molecule. In addition, a single miRNA molecule can target up to hundreds of mRNAs.

2.1.3 MiRNA detection technologies

The ideal biomarker for disease detection has to meet several criteria including disease specificity, the use of non-invasive protocols, an appropriate price-quality ratio and early diagnosis prior to the onset of clinical symptoms. The detection of miRNAs presence and concentration can be used for monitoring various diseases in the body. Thanks to the easy miRNA detection and amplification method, absence of post-processing modifications and sequence conservation between model organisms and humans, miRNA seems to be the ideal candidate for such biomarker.

There are several methods for detecting miRNA molecules, from which the best known are *i)* microarrays, *ii)* bead-based arrays and *iii)* quantitative real-time PCR.

The **miRNA microarray** is one of the most common and widespread techniques for miRNA detection. It is based on Watson-Crick base pairing and allows the simultaneous detection of hundreds of miRNA molecules. The principle of the microarray is following. Short oligonucleotide probes are immobilized on a glass slide to which a sample of miRNA molecules is added. Based on complementarity, the corresponding miRNAs hybridize to the probe. However, miRNA molecules are short and therefore it is difficult to standardize the melting temperature (T_m) of the probes without reducing specificity or sensitivity. The solution to this problem is using locked nucleic acids (LNAs). The LNA contains at least one monomer which is a "classical" nucleic acid analogue but the 2' oxygen atom and the 4' carbon atom of the ribose are "locked" by a methylene bridge.[23] The incorporation of one LNA increases the duplex T_m by an average of 5 °C.[24] As a result, it is possible to increase the T_m of all the probes even though the miRNA molecules are short. The microarray helped to identify miRNAs responsibility for some diseases and it potentially allows distinguishing between individual members of the miRNA family.

Another method for determining miRNA expression levels is the **bead-based array**, which uses carboxylated polystyrene microspheres containing a different mixture of two fluorescent dyes, since two fluorescent dyes are required for flow cytometry detection. Selected LNA probes are bound to the beads through COOH groups. Each microsphere with an LNA probe is

specific for a given miRNA molecule and this method can be used to distinguish between closely related members of the miRNA family. The analysis procedure is following. The miRNAs are isolated from the sample, biotinylated (to ensure high binding efficiency to the streptavidin) and subsequently hybridized to probes on the microspheres surface. The microspheres are then washed, incubated with streptavidin-phycoerythrin and analysed. Fluorescence analysis allows the identification of a specific miRNA based on a unique combination of a fluorescent dyes of the microsphere and the measurement of the streptavidin-phycoerythrin fluorescence intensity. This assay can be also used for quantitative analysis after constructing suitable calibration curve. The bead-based arrays also allow the simultaneous identification of hundreds of miRNA molecules.

The third mentioned technique for miRNA detection is a **quantitative real-time PCR**. Real-time PCR is a method based on the principle of classical PCR but it allows the quantification of the monitored DNA segment in real time (in conventional PCR, only the final product after completing all cycles is analysed). Here, a stem-loop primer, which binds to the miRNA molecule, is usually used.[25] Subsequently, a complementary DNA (cDNA) molecule (complementary to the miRNA molecule) is synthesized. The amount of the synthesized cDNA corresponds to the concentration of the probed miRNA and can be thus used for the detection instead of the miRNA. This cDNA is then detected by real-time PCR using a mixture containing a forward and reverse primer and a dual-labelled probe (TaqMan). The TaqMan probes are based on the 5' exonuclease activity of Taq polymerase during DNA synthesis. At the 5' end, it carries a fluorescent dye molecule and a quencher is binds at the 3' end. If cDNA is present, the probe binds to the cDNA and by the action of Taq polymerase the dye is separated from the quencher molecule and the fluorescence of the dye is detected. During PCR, with repeated cycles, the fluorescence signal gradually increases. Pre-miRNA molecules can be also detected by a real-time PCR when a suitable primer and probe are used.

A major challenge, however, lies in the detection and concentration measurement of miRNAs derived from a single miRNA family. These miRNAs differ in only one nucleotide yet they show different expression patterns. The largest known miRNA family contains nine members and they are *hsa-let-7a* to *hsa-let7i* (*a-i* members).[26] One way to solve this challenge is to use probes called molecular beacons.

2.2 Molecular beacons

Hybridization of a single-stranded nucleic acid with a complementary sequence is one of the most specific molecular recognitions. It gave rise to probes called molecular beacons (MBs), first reported by Tyagi and Kramer in 1996.[27]

MBs are single-stranded DNA probes consisted of a loop and a stem (see *Figure 2.2*). The loop is complementary to the target molecule and usually consists of 18 – 30 nucleotides. The stem is responsible for keeping the MB closed in the absence of the target molecule and usually consists of 5 – 7 nucleotide pairs (nucleotides that are complementary to each other). The stem is labelled at both ends with a fluorophore and quencher molecule, respectively. The fluorophore molecule is usually covalently attached to the 5' end of the MB and the quencher molecule is also covalently attached to the 3' end of the MB.

These oligonucleotide probes are designed to detect specific nucleic acids (complementary to the loop) in homogeneous solutions. The principle is as follows: In the absence of the targeted nucleic acid, MB is closed by the stem, which brings the fluorophore molecule close to the quencher molecule decreasing the fluorescence emission. However, upon binding of the target nucleic acid, the conformation changes. The MB opens and the fluorophore molecule moves away from the quencher molecule, which is detectable by an increased fluorescence intensity.[28]

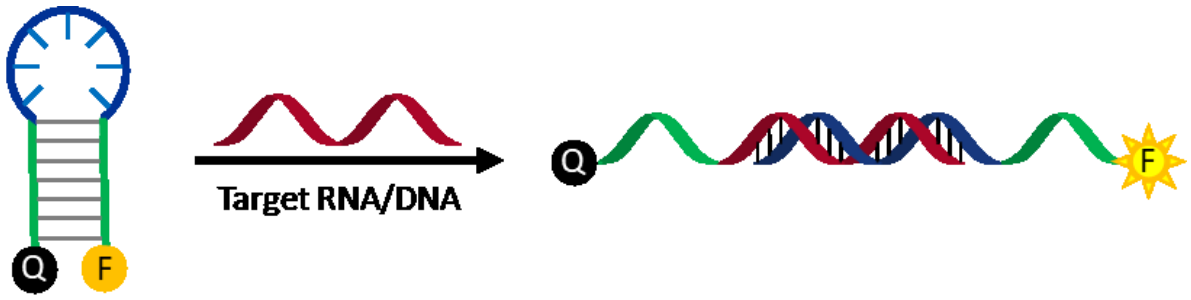

Figure 2.2: Basic principle of molecular beacons

MBs are characterized by high specificity, selectivity, and easy operation, which makes them very popular group of probes for the detection of various nucleic acids across fields of chemistry, molecular biology or biomedicine.[29,30]

2.2.1 Design principles of molecular beacons

The whole process of proper MB design begins with the selection of a loop sequence (sometimes called a probe sequence) that is responsible for the specificity of the whole system.

In the case of PCR product detection, the entire probe should be long enough to specifically bind the target molecule at annealing temperature. In order to use MB to distinguish a target molecule from a molecule that differs from it by only one nucleotide, the length of the loop sequence should be such that it dissociates from its target molecule at temperatures 7 – 10 °C higher than the PCR annealing temperature.[31,32] The "percent-GC" (guanine and cytosine) rule or the "nearest neighbour" rule are most commonly used to predict the melting temperature of the target molecule-loop duplex, which is also used by some available online programs.[33] This prediction should be made before selecting the stem sequence.

On the other hand, if it is not necessary to distinguish between molecules that differ in one nucleotide, it is possible to use longer and thus more stable loop sequences. Although, the specificity of the longer sequences is lower, such probes have increased affinity. The sensitivity and specificity of the loop sequence for the target molecule can be optimized not only by the length of the probe sequence but also by the guanine and cytosine content (GC content).

In general, the length of the loop sequence should be at least twice the stem length to achieve sufficient separation of the fluorophore from the quencher upon binding of the target nucleic acid. The ideal length of the loop sequence is 15 – 30 nucleotides with requirement that the loop does not form any secondary structures.[27,32]

The second step in MB design is to design the stem by attaching two short, mutually complementary sequences on the both ends of the loop sequence. The stem usually consists of 5 – 7 base pairs and has a very high GC content (75 – 100 %).[34] A properly designed stem has a melting temperature about 7 – 10 °C higher than the temperature at which detection of the target nucleic acid will be performed.[35]

In the case of use of the MB for detection nucleic acid associated with PCR, the length and GC content of the stem are designed according to the annealing temperature. The main requirement is that in the absence of the target molecule, the stem keeps MB in a closed conformation.

Because the stem is formed by intramolecular hybridization, its melting temperature cannot be predicted using the percent-GC rule. However, in general, a stem containing 5 GC pairs has a

melting temperature between 55 and 60 °C, 6 GC pairs in the range of 60 and 65 °C and a stem containing 7 GC pairs has a melting point between 65 and 70 °C.

However, the length of the stem needs to be also considered. In general, MBs, which have a shorter stem, have faster hybridization kinetics. A longer stem can increase the difference in the melting temperature of the duplex of an ideally complementary target molecule and mismatched molecule. It follows that MBs with a longer stem have higher specificity, better signal-to-background difference but slower kinetics.[36]

Another important aspect of the design is the selection of the appropriate nucleotide binding the fluorophore molecule. It has been found that this nucleotide quenches the fluorophore fluorescence.[37] By comparing the individual nucleotides, it was found that guanine is the worst choice, closely followed by adenine, while thymine and cytosine show significantly less quenching efficacy. The explanation for the greatest effect of guanine is that guanine is able to donate electrons, which causes energy transfer between the fluorophore and the base. Another finding is that blue- and red-emission fluorophores are less successfully quenched than yellow- or green-emission fluorophores. Though these aspects have lower impact on fluorescence compared to quencher, still affect the behaviour of MBs and should be considered when designing.

Consequently, it is necessary to verify whether the MB (stem-loop structure) designed in this way forms a hairpin structure in the absence of the target molecule.

The last step is to select a pair of a quencher and fluorophore. The proper selection of the fluorophore quencher pair is essential to achieve the appropriate signal to background ratio. Several studies have been performed investigating the suitability of individual quenchers for different fluorophore molecules.[37] A wide selection of fluorophores is currently available allowing a safe coverage of the entire visible spectrum (from 400 to 700 nm).

The fluorophore is usually selected according to the design of the whole experiment and on the basis of the available instrumentation. Subsequently, a suitable quencher is selected according to the fluorophore in order to obtain the highest possible quenching efficiency in the absence of the target molecule.

The three most commonly used universal quenchers are Dabcyl (4-(dimethylaminoazo)benzene-4-carboxylic acid), Black Hole Quenchers 1 (BHQ-1) and Black Hole Quenchers 2 (BHQ-2).[37] Their versatility lies in the fact that they are suitable for most of

the used fluorophores and usually guarantee a static quenching efficiency from 80 to 98 %. Moreover, BHQ-1 and BHQ-2 are static quenchers, therefore the spectral overlap of the fluorophore emission band with the quencher absorption band and different coloured fluorophores can be quenched by these quenchers. For example, BHQ-1 has maximal absorption at 534 nm but successfully quenches fluorophores from visible to near infrared region.[38]

It has been found that the choice of fluorophore quencher pair affects melting temperature.[37] For example, the stem-loop structure can have a melting temperature of 49 °C, but depending on the pair of fluorophore and quencher, the melting temperature can vary from 51 to 59 °C. An important finding is that fluorophore-quencher pairs that, increase the melting temperature more, have higher quenching efficiency.

2.2.2 Synthesis of molecular beacons

One of the most widely used methods for MB synthesis is solid-phase synthesis using phosphoramidite method.[28,39] The name of this method is derived from phosphoramidite, which consists of various functional groups (see *Figure 2.3*). The black colour represents the sugar ring, the blue is a nitrogen base and the phosphate is highlighted in green. A di*iso*propyl phosphoramidite group (purple colour) is attached to the 3' OH group of the sugar ring, which serves as a protecting group and simultaneously ensures efficient coupling. To prevent side reactions, a 2-cyanoethyl group (orange colour) protects phosphite. The 5' OH group of the deoxyribose is capped with a dimethoxytrityl group (red colour). This group is sensitive to acidic environments and therefore can be selectively activated during synthesis under acidic conditions. All NH_2 groups of the nitrogen bases are also protected by forming an amide with the corresponding acyl. These protecting groups can be removed using a strong base.

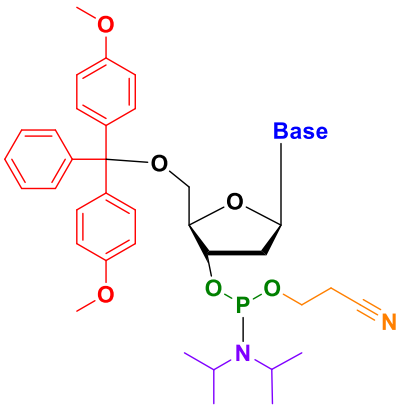

Figure 2.3: Structure of phosphoramidite

Oligonucleotide synthesis proceeds from 3’ to 5’, while enzymatic nucleic acid synthesis proceeds from 5’ to 3’. Briefly, the first nucleotide is covalently linked to the solid support of column (which contains a controlled pore glass bead with holes and channels) via a 3’ hydroxyl group. One synthetic cycle involves four steps (chemical reactions). The whole synthetic process takes place on a column, which allows easy exchange of reactants and subsequent removal of by-products.

The first step is **detritylation**. The column is washed with an acidic pH solution (trichloracetic acid), thereby removing the trityl protecting group on the 5’ OH group. This hydroxyl group is now the only functional group capable of reaction with the next nucleotide. The second step is **coupling**, in which a phosphoramidite derivative of the second nucleotide together with tetrazole is added to the column. The tetrazole is a weak acid and causes the protonation of di*iso*propylamine of the second nucleotide. It thus facilitates the nucleophilic attack of the free 5’ OH group of the first nucleotide to the phosphorus atom of the second nucleotide, to form an unstable phosphate triester linkage.

However, the second step does not proceed in 100 % yield, which means that there are still some free 5’ OH groups that could react in further cycles, leading to the formation of undesired oligonucleotides. To prevent this, the third reaction step is **capping**, which captures unreacted 5’ OH groups by acetylation. This is done using acetic anhydride and 1-methylimidazole. The fourth step is **oxidation**, which converts less stable phosphite to more stable phosphate linkage. A mixture of iodine, which serves as an oxidizing agent, water, as an oxygen donor, and pyridine, as a weak base, is used for the oxidation.

The MBs still need to have a fluorophore and quencher molecule covalently attached to the 3’ and 5’ end. For this synthesis, the above-mentioned protocol is slightly modified. The difference is in the use of a solid support, which is derivated with a quencher molecule at the 3’ end. This allows MBs to be synthesized with Dabcyl, BHQ-1 or BHQ-2. Subsequently, the following nucleotides are added. The last nucleotide is derivated at the 5’ end with a fluorophore molecule. The fluorophore and quencher are usually attached via amino or sulfhydryl groups at each end.

In most cases, no changes of the synthesis protocol are necessary for the 5’ fluorophore attachment. However, sometimes fluorophores have to be attached post-synthetically. In this case, phosphoramidite with amino or sulfhydryl group is used as the last nucleotide. If the amino group is used, the succinimidyl ester fluorophore derivative is most often selected for this purpose. In the case of the sulfhydryl group, either fluorophore iodoacetamide or

maleamide derivatives are prefered. If it is possible to remove the amino or the sulfhydryl protecting group of the phosphoramidite group without affecting the whole oligonucleotide, the reaction with the fluorophore takes place directly on the column. If this is not possible, the resulting oligonucleotide is first removed from the column, purified by HPLC, and the fluorophore attachment reaction is performed in solution. However, this requires subsequent HPLC purification leading to a lower yield of the whole synthesis.

Finally, it is necessary to remove all protecting groups from the formed MBs and the 2-cyanoethyl group on the phosphate. Unlike conventional oligonucleotides, MBs require special attention because some deprotection methods can irreversibly damage the fluorophore.

2.2.3 Characterization of molecular beacons

Newly synthesized MBs needs to be appropriately characterized. Mass spectroscopy is the basic method of characterization, which allows to confirm the correct structure of MBs according to molar mass. However, in addition to this method, it is necessary to determine the signal-to-background ratio (SBR) and thermal denaturation profile.[28,29]

The SBR reflects the purity of the prepared MBs as well as the appropriate design. The low SBR usually means insufficient purity of MBs, which is often due to the presence of oligonucleotides with a fluorophore but without a quencher.

The SBR is determined by a spectrofluorometer and ideally, MB should have this ratio higher than 20. First, the fluorescence value of the buffer (F_{buffer}) is measured. Then, a certain amount of MBs is added to achieve a suitable MB concentration (usually 50 – 200 nM). Low concentration would result in low measurement sensitivity, high concentration in self-quenching. The fluorescence value of the closed MB, denoted F_{closed}, is then measured. Subsequently, a five-fold molar excess of the target molecule, which is perfectly complementary to the MB loop sequence, is added and the new fluorescence value, F_{open}, after stabilization is determined. The whole measurement is performed at a constant temperature. The signal-to-background ratio is calculated as follows:

$$\text{SBR} = \frac{F_{\text{open}} - F_{\text{buffer}}}{F_{\text{closed}} - F_{\text{buffer}}} \quad (1)$$

Additionally, the effect of temperature on the fluorescence properties needs to be determined. Temperature plays an important role in the MB behaviour because higher temperature weakens

the hydrogen bonds between complementary bases in the stem and thus opens MB in the absence of the target molecule.[34] The temperature dependency is measured by gradually heating the solution containing MBs in the absence of the target molecule. This measurement is then repeated with the target molecule that is fully complementary to the MB loop sequence in the solution for comparison. Often, mismatched target are tested as well.[40]

Ideal thermal profiles should look as follows: In the absence of the target molecules, MB forms a stable hairpin structure at low temperature, as the fluorophore and quencher are close to each other and thus only background fluorescence is observed. At a higher temperature, the thermal motion of the chain will be greater than the attractive hydrogen bonds between the stem nucleotides and a random-coil configuration will take place, causing separation of the fluorophore from the quencher and a significant increase of the fluorescence value. The melting temperature depends on the length of the stem, the GC content as well as the ionic strength of the buffer.

The situation is opposite in the presence of the target molecule. The target nucleic acids hybridize with the MB loop sequences resulting in a high value of fluorescence at low temperature. With increasing temperature, the fluorescence remains stable until at a certain point, after which decreases sharply. This decrease is due to the dissociation of the target molecules from MBs and thus the transition of MBs to a closed state, where the fluorophore and quencher are in close proximity. The temperature at which the target molecule-MB duplex melts depends mainly on the length of the probe sequence and the GC content.

Using a mismatched target, the temperature dependence of the fluorescence is similar to that of the target molecule but the decrease in fluorescence occurs at a lower temperature. The knowledge of the thermal denaturation profile is important for the selection of a suitable temperature interval where MB hybridization solely with the target molecule occurs, but not with the mismatched target. Based on these measurements, the highly selective potential of MBs as the probes for nucleic acid detection is demonstrated.

2.2.4 Application of molecular beacons

MBs have found use in all fields, where short nucleic acids need to be detected very sensitively and selectively. One of the widely used applications of MBs is real-time PCR. The **real-time PCR**, also called quantitative PCR (QPCR), is a technique that uses conventional PCR but allows the detection of products even during the amplification reaction. This is possible by the

incorporation of a fluorescent element into classical PCR. The undeniable advantage of QPCR is that it is not necessary to wait for all the cycles to completely finished, as the products can be identified much earlier, thus saving time.

There are two main ways to obtain a fluorescent signal from PCR products. The first one is based on DNA binding dyes, such as SYBR Green I, which bind non-specifically to the DNA double helix, increasing its fluorescence.[41] The second option is the use of fluorescence probes (such as MBs). This approach is definitely more sensitive and selective. In probe-based chemistries, almost all probes contain a quencher that is close to the fluorophore (often a report dye) and quenches its fluorescence. As products are formed during PCR, the linkage between the quencher and the fluorophore is broken, leading to an increase in fluorescence.

MBs are ideal probes for the detection of short oligonucleotides and are therefore well suited for real-time PCR.[42] The MBs hybridize to the template DNA in an annealing step, thereby increasing their fluorescence. In a subsequent extension step, the polymerase synthesizes the sequence, displacing the MB and returning it to its closed conformation. The advantage of this approach is that the MBs can be reused in the next cycle again. MBs should be designed to hybridize at a temperature 7 – 10 °C higher than the primers to ensure detection before the primers are extended. The use of MBs in QPCR is very simple, fast, sensitive and even allows the detection of multiple nucleic acids simultaneously using different probes. Their advantage over the commonly used TaqMan probe[43] is that MBs do not require a polymerase with exonuclease activity.

Furthermore, a detailed comparison of the MBs with other probes[44] found, that MBs have better specificity than TaqMan and they are less design-intensive than the Scorpion probe,[45] making them ideal candidates for instance for single-nucleotide polymorphisms (SNPs) analysis. The human genome consists of a large number of SNPs. While many of them do not affect health, there are also those that are responsible for certain diseases. A key requirement for SNPs detection is recognition between a perfectly complementary target molecule and a single-base mismatch target. As mentioned above, only properly designed MBs can do this. Moreover their temperature window is wider compared to the corresponding linear probes.[36]

Another MB application was proposed by Kramer et al. as early as 1998, only 2 years after MB discovery, was reported.[42] They have demonstrated a method for spectral genotyping of human alleles using differently labelled MBs. In this technique, one type of MB (with the green fluorophore) is used for the wild type allele and the other (with the red fluorophore) for the

mutant allele. Depending on whether red, green or both signals are detected, homozygous wild type, homozygous mutant and heterozygote, respectively, can be recognized.

Furthermore, four MBs labelled with a fluorophore of different colour were used simultaneously to correctly detect four different alleles that varied by only one nucleotide position.[46] Each of the four tubes contained only one target allele, but all four MBs were added to each tube. After PCR, only one fluorescence colour was detected in each tube. This experiment demonstrates the exceptional specificity of MB.

MBs are most often detected optically based on the change in fluorescence before and after binding of the target molecule.

2.3 Quantum sensing

In recent years, quantum sensing appeared as novel perspective research field. Generally, quantum sensing means applying a quantum system and its quantum properties to measure a physical quantity. Thanks to the high sensitivity and accuracy of quantum sensing, it opens up new possibilities not only in physics, but also in other natural sciences, including chemistry, biochemistry, biology, and medicine.

However, the definition of quantum sensing is often more complex. In practice, we encounter the three most common possibilities: (I) The use of a quantum object to measure a physical quantity. (II) The use of quantum coherence to measure a physical quantity. (III) The use of a quantum system to improve the accuracy or sensitivity of a measurement, as opposed to the use of the classical (non-quantum) method.[47] The first two of these definitions are quite broad and cover several systems, while the third definition is stricter. On the other hand, many applications using quantum sensing follow the first two definitions.

A quantum system is a system that has discrete energy levels. For simplicity, we will consider a system with two energy levels $|0\rangle$ and $|1\rangle$ that are separated by $E = \hbar \cdot \omega_0$ (see *Figure 1.4*). At the same time, it must be possible to initialize the system to a known state, which can be read out and we must be able to manipulate this system. The quantum system most often reacts to a change in the electric or magnetic field, which is expressed for instance by energy level shift or by a change in the transition rate (e.g. electron spin coherence time) between the energy levels.

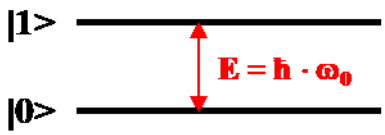

Figure 2.4: Basic structure of two-state quantum system

2.3.1 Optical quantum nanosensors

The advancement in nanotechnologies in the last twenty years gave rise to optical nanosensors. These nanoscale probes can be used to measure various quantities, such as temperature, pH or the presence of certain nucleic acids inside cells in extremely low concentrations. They have opened up new possibilities across the field of chemistry and biomedicine. For example, many processes in cancer cells are associated with local heat production[48] and extracellular acidic pH.[49] Luminescent probes can be used to visualize and understand metabolic processes in healthy and diseased cells.[50] Compared to conventional probes, nanoparticle probes excel in increased photostability, sensitivity and versatility. Coating their surface can significantly improve their biocompatibility and prevent non-specific interactions, but also allows the attachment of specific molecules for improved nanoparticle transfer into cells or cell targeting.

Nanosensors can be nowadays fabricated to host optical quantum defects that meet the quantum sensing criteria. Such quantum probes then need to meet several requirements in order to be used effectively for quantum sensing in biological environments (e.g. inside cells). First, they have to be biocompatible. Second, their observed parameters (fluorescence intensity, electron spin coherence time, wavelength, lifetime, etc.) have to depend suitably on the change of the monitored quantity. At the same time, they have to be durable with respect to the probed environment.[51] Crucially, their detection and readout must be possible with sufficient sensitivity. The drawback of many optical nanosensors is the need of shortwave radiation (to induce transitions between the energy levels), which is scattered in a biological system and can be also harmful for the cells (e.g. heating).

The quantum readout of the optical nanosensors is done by monitoring the change of its optical properties (i.e. fluorescence). When designing and intracellular optical nanosensor, one should consider the type of the probed cells since the uptake into cells significantly depends on the cell type. For example, macrophages are willing to accept all types of particles, while other cells are virtually immune to particle uptake.[52]

Optical quantum probes can be employed for temperature sensing, which is a crucial for cell biology as it reflects the ongoing metabolic processes in the cells. Increased temperature often signals disease processes. Therefore, it is important to be able to accurately and in real time measure the temperature locally inside the cells. For cell temperature sensing, several approaches have been proposed. The standard procedure is the use of constant thermoelectric sensors,[53] which, however, have a limited resolution compared to fluorescent nanoprobes and are often invasive.[54] Probes based on thermoresponsive polymers, that change their hydrodynamic radius with temperature, such as poly (*N-iso*propylacrylamide) (pNIPAM), seem to be relatively promising. These polymers has to be used in connection with a suitable carrier[55] and localized intracellular sensing have not been demonstrated yet.

Optical probes have been also demonstrated for pH sensing. Compared to temperature, pH can vary significantly inside cells and in the extracellular space. that the detection of a localized pH difference is of high importance, as any pH deviation may signal a disease.[56] The proper pH is also necessary for ion transport, endocytosis or response to therapies.[57] pH-sensitive fluorescent dyes[58] or pH sensors based on lanthanoide upconversion nanoparticles can be used to measure intracellular pH.[59] These nanoparticles are excited by a lower energy photon while a high energy photon is emitted.

Inorganic nanoparticles, which should definitely not be forgotten in quantum sensing, are fluorescent nanodiamonds (FNDs).[54] The use of FNDs in quantum sensing lies in the lattice defect of nanodiamonds called nitrogen-vacancy (NV) centres.[60] The electronic structure of these NV centres has distinct magnetic levels and individual transitions between electronic states can be affected by the surrounding environment even at room temperature. The fluorescence value of nanodiamond NV centres is extremely constant and does not suffer from photobleaching. Another huge advantage of FNDs is their high biocompatibility. Therefore, FNDs have found application in quantum sensing, for example to detect changes in magnetic field fluctuations, temperature or pH with unprecedented sensitivity.[61]

2.4 Nanodiamonds as quantum probes

At the end of the 18th century, a French chemist Antoine Lavoisier and English chemist Smithson Tennant independently proved that diamond and graphite are carbon allotropes. Since then, diamonds have started to attract even more attention. It is well-know that diamond is the

hardest mineral ever[62] thanks to the strong covalent bonds between carbon atoms (each carbon atom bonds to four adjacent carbon atoms). In combination with its excellent thermal conductivity[63] and almost zero electrical conductivity, it is straightforward that diamonds are desired for various applications.

Over the last century, attention has been drawn to the synthesis of nanodiamonds (NDs). NDs possess the exceptional properties of diamonds while their surface is several times larger. This large surface-to-volume ratio of NDs is beneficial for surface modification and subsequent attachment of a large number of molecules (as explained further in *part 2.4.4*), which is particularly useful for biosensing application.[64]

Of all existing carbon nanomaterials, nanodiamonds are exceptional thanks to their good biocompatibility and low toxicity, which are associated with the chemical inertness of the diamond core. Moreover, NDs contain a large number of different surface functional groups, which can be used for non-covalent or covalent attachment of various biomolecules or drugs, or incorporation of NDs into different composite biomaterials.[65] ND particles can be modified to host very stable fluorescent centres embedded in the diamond lattice, which thus do not suffer from photobleaching, making them promising candidates for *in vitro* and *in vivo* imaging. The size of some NDs can be even below 5 nm allowing potential penetration through the smallest pores in the body, such as the cell nuclear membrane or blood-brain barrier. Thanks to these unique features, NDs stand out from other nanoparticles, which usually do not possess the combination of so many important properties. Moreover, NDs can be produced in large quantities at an affordable price.

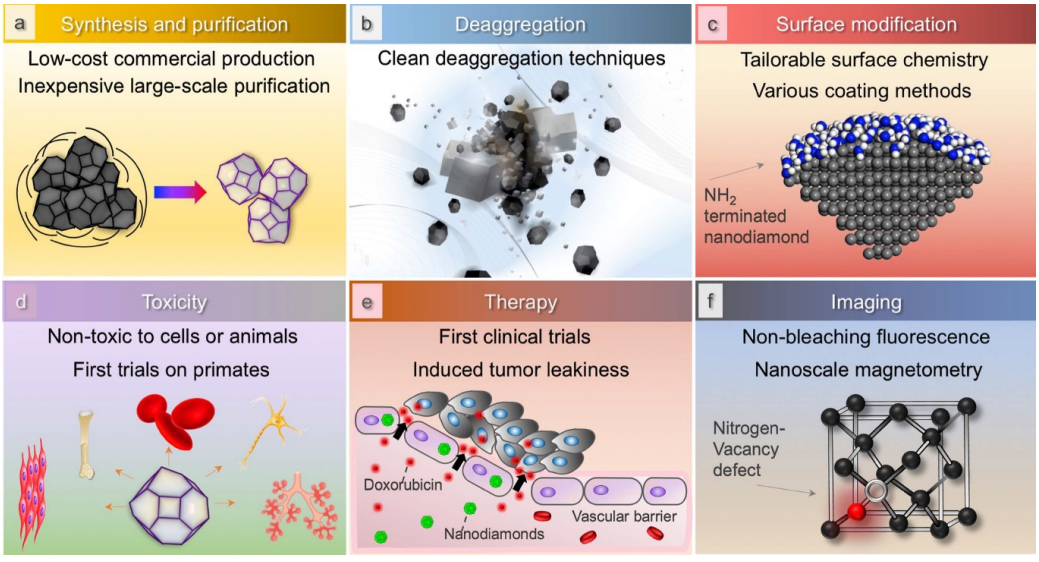

Figure 2.5: Schematic representation of some nanodiamonds advantages. Picture adopted from.[64]

2.4.1 Preparation of synthetic nanodiamonds

The first natural diamonds were discovered in India about 3 000 years ago but they have been probably known for 6 000 years.[66] In the course of the 20th century, several procedures have been developed for the nanodiamonds synthesis, among which the most significant and widespread are detonation, high-pressure high-temperature and chemical vapour deposition. These three approaches are discussed below. Each of these methods leads to the preparation of nanodiamonds with different size, purity and properties.

The oldest synthetically prepared nanodiamonds are **detonation nanodiamonds** (DNDs). They were synthetized in the early 1960s in the territory of present-day Russia (back then the USSR). Nowadays, DNDs are prepared by a controlled explosion of certain organic compounds in a closed chamber.[67] For instance, a mixture of TNT and hexogen (see *Figure 2.6*) is used as a typical explosive mixture. Since during the explosions, an enormous amount of heat is released, the reaction takes place in the presence of a non-oxidizing cooling agent that is stable at high pressures. The cooling medium used media can be gaseous (e.g., argon and carbon dioxide) or water (ice). Accordingly, detonation synthesis is divided to "dry" and "wet", respectively. To reduce graphitization of the created DNDs at the high temperatures generated during the explosion, the cooling rate must be at least 3000 K per minute.[68] As the detonation wave passes through the material, a temperature reaches typically 3500 to 4000 K and a pressure of 20 to 30 GPa is generated, which corresponds to the phase region for the formation of thermodynamically stable nanodiamonds.[69]

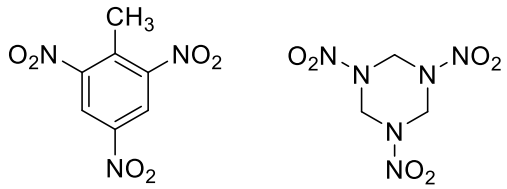

Figure 2.6: Structure of TNT and hexogen

However, this preparation method yields nanodiamonds coated with a layer of amorphous carbon and post-synthetic purification is necessary to prevent their non-specific aggregation. Most of the impurities come from the chamber material, which is released during the explosion, or from used initiator (most often lead, copper and silver azides).

The size of the prepared DNDs depends mainly on the weight of the explosive charge (the explosion conditions) and there is no specific maximum size. Typically, DNDs are uniform with up to 5 nm in size and oval shape.[67] Thanks to their small proportions compared to

nanodiamonds prepared by other techniques and the narrow size distribution, DNDs are widely studied for biomedical applications.[70]

The surface of the prepared DNDs is to some extent chemically inert, but is reactive enough to be subsequently functionalised. Because of the large surface area, it is possible to modify DNDs with numerous different functional groups, making them promising candidates for use in drug delivery. On the other hand, DNDs suffer from a lack of stable lattice defects.[71] Although, recent studies have demonstrated the use of DNDs for labelling employing alternative approaches. Thanks to the tuneable rich DNDs surface chemistry, the desired optical properties reaching high intrinsic photoluminescence can be achieved.[72] Alternatively, they can act as a support for dyes.[73]

In addition to the fluorescence associated with lattice defects, nanodiamonds also exhibit another type of fluorescence from the amorphous carbon layer and graphite shells on the nanodiamonds surface. This layer can quench the fluorescence of the colour centres,[74] which is encountered particularly in DNDs. As a consequence, the surface fluorescence may be more intensive, than the fluorescence of the colour centres.[75] To prevent this, several purification procedures, based on the selective oxidation of sp^2 carbon atoms to sp^3, have been proposed.[76]

The second type of nanodiamonds is **high-pressure high-temperature** (HPHT) NDs. Today's apparatuses for HPHT synthesis consist of three main parts. The first is a chamber made of pyrophyllite (a mineral composed of aluminium silicate hydroxide that has excellent thermal stability and can withstand very high pressures) with a metal sample tube inside. Pyrophyllite provides pressure transfer to the sample tube as well as thermal and electrical insulation. The second part is a press that is responsible for generating high pressures and temperatures required for diamond formation. The last part is molten metal (most commonly nickel), which dissolves a carbon source (such as graphite) and allows diamond crystallization. Liquid phase oxidative treatment, which is based on the action of strong oxidizing acids (such as sulfuric, nitric, perchloric acid or a mixture thereof in a suitable ratio), can be used to remove graphite residues or metal impurities.[77]

Prepared diamonds are then grinded down, using high energy ball milling, to nanoparticles of the desired size.[78] Using this method, it is possible to prepare nanoparticles of uniform size in the range of few nm to ~ micrometre. Due to the use of abrasives, the nanodiamonds grinding is relatively inexpensive and it allows large-scale production. To obtain HPHT NDs smaller than ~ 10 nm, the colloid solution of the smallest commercially available NDs can be

centrifuged filtering the larger NDs in the pellet while keeping the smaller NDs in the supernatant.

Compared to DNDs, HPHT NDs can host several stable crystal defects in their structure, of which nitrogen vacancy (NV) centres are best-known and the most studied and can be artificially created in the various quantities (see *part 2.4.2*). HPHT NDs are thus suitable for optical labelling and widely used for quantum sensing applications. The surface of HPHT NDs also contains a wide variety of functional groups that can be further modified.

Chemical vapour deposition (CVD) is the third most widely used technique nanodiamond synthesis.[79] Compared to the previous two methods, which require inevitably very high pressures, CVD nanodiamonds are produced at low pressures.

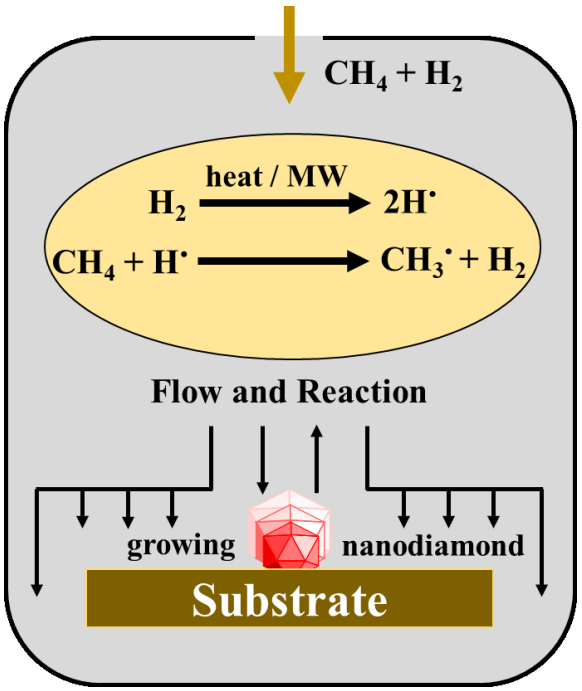

Figure 2.7: Scheme of basic processes in CVD technique.

The *Figure 2.7* shows schematically the preparation of nanodiamonds by the CVD process. The gas chamber contains the substrate with a seed – a small molecule unit with a diamond crystal structure such as diamondoid. The seed serves as a precursor for nanodiamonds grow.[80] Nucleation is followed by the growth of individual nuclei in all three diameters until they coalesce to form a continuous film (sometimes non-diamond carbon is incorporated into this structure).[81] First, feed gas (such as methane or acetylene), which serves as a carbon source, is mixed with hydrogen gas typically in a ratio of 1:99. Using heat or microwave radiation, the hydrogen molecule is split into two hydrogen radicals. These react with the methane molecule

to form a methyl radical and a hydrogen molecule, allowing the reaction to proceed cyclically. The sp^3 diamond is formed atom-by-atom, layer-by-layer, whereas the sp^2 carbon is removed in the process.

The preparation of nanodiamonds by CVD technique is a kinetically driven process, not thermodynamically, which means that graphite is the favourable product under CVD synthetic conditions but nonetheless, nanodiamonds are formed. This is possible due to the very reactive hydrogen radicals, which play a key role in this process – they etch away sp^2 carbons of graphite from the substrate surface while keeping the diamond carbons. The CVD process allows a high degree of freedom, since parameters such as the composition of the gaseous mixture, temperature or the method of forming process initiation by plasma can be tuned in different ways.

Although this preparation technique allows to prepare nanodiamonds with a high-quality lattice structure, the obtained yield is very low, which enormously increases the preparation costs. For this reason, HPHT are the most common type of nanodiamonds for quantum sensing applications.

2.4.2 Nitrogen-vacancy centres

The colour of diamonds is strongly influenced by the type of impurities in the crystal lattice. It is important to note that pure diamonds without any foreign atoms are colourless. Lattice defects consisting of one or more impurity atoms or vacancies, which exhibit fluorescent behaviour, are called colour centres. Each colour centre is unique, thanks to its optical properties and therefore can be identified on the basis of the emission or absorption spectrum. There are more than one hundred well-known colour centres in diamond.[82] These colour centres have been the subject of various studies for a long time, first in natural diamonds and since the 1950s, attention has been focused on colour centres in synthetic nanodiamonds.

An interesting attribute of many of these diamond colour centres is their extreme stability.[83] Of all the known colour centres, the **nitrogen-vacancy (NV) centres** attract the most attention due to the fact, that they have a spin triplet and can be read and initialized to a defined state optically at room temperature. Their fluorescence is associated with a spin state, which means that the fluorescence intensity can be modulated by the microwave field. The stable fluorescence of the nanodiamonds NV centres and the size of only a few nanometres have attracted attention across various scientific disciplines.

As the name suggests, the NV centre consists of a nitrogen atom and an adjacent vacancy in a crystal lattice. Most of the HPHT NDs can already contain a NV centres in some of the particles. For example, in a sample of commercially available HPHT nanodiamonds with an average size of about 25 nm, the NV centres are present in less than one particle per thousand.[84] This amount is too low for practical use and therefore ways have been developed to increase the number of nanodiamonds with NV centres. Irradiation of nanodiamonds with high-energy particles (most often electrons or protons) and annealing at a temperature higher than 800 °C are the two most commonly used methods to increase the number of NV centres. During irradiation, carbon atoms are knocked creating new vacancies. The high temperature annealing supports the creation of the new NV centres. At a low temperature, the vacancies are immobile. During annealing, thanks to thermal diffusion, vacancies pair with the nitrogen atoms that are already present in HPHT crystals, forming new NV centres.

Figure 2.8 shows the structure of the NV centre. It consists of 6 electrons. The nitrogen atom provides two electrons and another three electrons come from three adjacent carbon atoms. The last sixth electron is captured from the lattice donor and causes a negative charge of the NV centre. In addition, there are also NV centres with a positive or zero charge, however these are not magnetically-optically active but they are very important for various applications including sensing based on charge-switching or photoelectric readout. Since this work is focusing only on the application of the negatively charged centres, the "NV" from now on stands for the negatively charged centres unless stated otherwise.

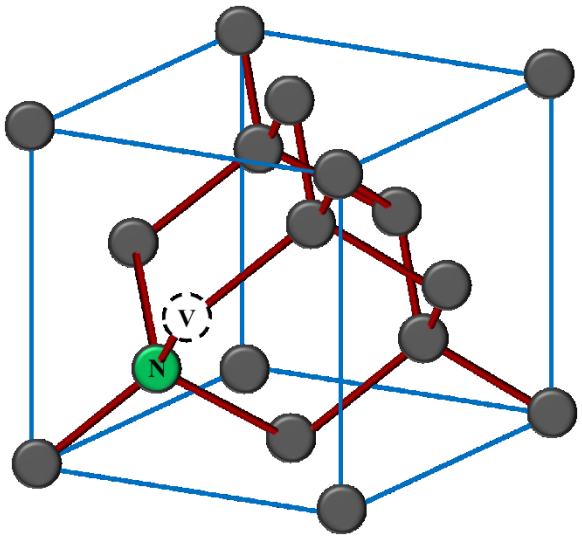

Figure 2.8: Structure of the NV centre. Grey points represent carbon atoms, the green point is a nitrogen atom and V stands for vacancy.

In order to understand the optical properties of NV centres, it is necessary to understand its electronic structure. *Figure 2.9* represents a simplified energy diagram of the NV centre in the diamond bandgap, describing all the important magneto-optical transitions. The NV centre has a ground state (GS) triplet with $^3A_2$ symmetry. The corresponding excited state (ES) with ^3E symmetry is separated by 1.945 eV and is also a triplet with the total spin of one. The singlet metastable state (MS) has a ground and an excited state with ^1E and $^1A_1$ symmetry, respectively.

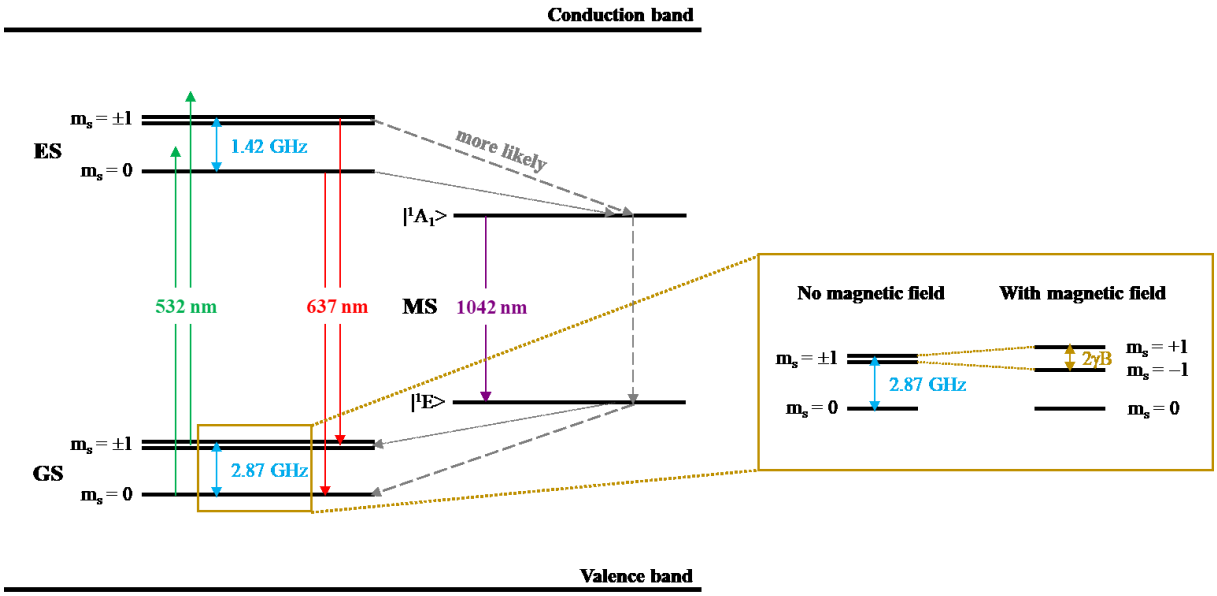

Figure 2.9: Energy-level diagram of the NV centre

The main electron transition between the triplet ground and the excited state is called the zero phonon line (ZPL) and has a wavelength of approximately 637 nm, which corresponds to the red region of visible light (see *Figure 2.9*). However, only a few percent of the electrons are emitted in the ZPL and most of the fluorescence takes place in vibrational phonon side bands in the wavelength range from ~ 630 to ~ 800 nm. The average lifetime of the excited state is only about 13 ns for the NV centre in the bulk diamond, while the lifetime of the metastable singlet state is incomparably longer and it is about 250 ns.[85] Nanodiamonds are also unique in the quantum yield of fluorescence, which is close to 100 %.[86] This fluorescence is relatively strong and excellently stable allowing detection of even single NV centre. Moreover, the NV fluorescence lifetime is much longer than the autofluorescence of tissues – about 20 ns compared to 3 – 4 ns[86], and almost 70 % of the emitted radiation falls in the near-infrared window of the biological tissue.

The ground state and excited state triplets consist of an energetically lower sublevel with spin $m_s = 0$ and energetically higher sublevels $m_s = \pm 1$. The energy difference between the sublevels

$m_s = 0$ and $m_s = \pm 1$ at zero magnetic field, so called zero-field splitting (D), is D = 2.87 GHz for the ground state, while D = 1.42 GHz for the excited state. The sublevels $m_s = \pm 1$ are degenerate at zero field due to axial symmetry of the $m_s = +1$ and $m_s = -1$ states. However, this degeneration is lifted in the presence of a magnetic field, which causes the sublevels $m_s = +1$ and $m_s = -1$ to orient in opposite directions and separate. The energy difference (ΔE) between these two sublevels is linearly dependent on the magnetic field (B) such as $\Delta E = 2\gamma B$, where γ gyromagnetic ratio.

The metastable singlet state plays a key role in the magneto-optical properties of the NV centre. As depicted in *Figure 2.9*, from the excited state the electrons can fall back directly to the ground state through fluorescent spin-preserving[87] transition or, alternatively, they can decay through the metastable state without emitting the red photon (also called dark transition). The $m_s = \pm 1$ electrons have higher probability to decay non-radiatively via the dark transition and to be shelved in the long-lived metastable state, thus not contributing to the fluorescence. This creates an optical contrast of approximately 30 % between the $m_s = 0$ and $m_s = \pm 1$ sublevels. The electrons that decay trough metastable state are more likely to fall back to the $m_s = 0$ ground state, thus, after several optical cycles, the NV are polarized to the $m_s = 0$ state.

2.4.3 Quantum sensing using nanodiamonds

The idea of quantum sensing is to monitor slight environmental changes, such as magnetic or electric field changes, trough the change of the optical properties of NV centres. These magneto-optical properties of NV centres can be monitored using a technique called optically detected magnetic resonance (ODMR). The ODMR is a double resonance technique which optically detects transitions between individual spin sublevels.[76] As mentioned above, the fluorescence lifetime, and thus the intensity of the fluorescence, strongly depends on the spin state of the NV centre electrons.

Spin-dependent fluorescence can be thus used ODMR experiments. The principle of this method is following. Using a microwave (MW) radiation with a appropriate frequency, the electrons can be flipped between the $m_s = 0$ and $m_s = \pm 1$ sublevels. By sweeping the frequency of the MW field, while simultaneously optically exciting the NV centre, a dip can be seen in the PL signal for the resonant frequency. *Figure 2.10* (left) shows such ODMR spectrum of the fluorescence intensity as a function of the MW frequency. The spectrum was measured in the absence of a magnetic field. A decrease in fluorescence intensity can be seen at a frequency of

approximately 2.87 GHz corresponding to the $m_s = 0$ and $m_s = \pm 1$ transition (zero-field splitting). When a magnetic field is applied, two dips are visible in the ODMR spectrum (see *Figure 2.9 – right*). They correspond to the resonant frequencies of the transitions from the sublevel $m_s = 0$ to the $m_s = +1$ and to the $m_s = -1$ respectively, because after the application of the magnetic field, the spin sublevels are split by a $2\gamma B$.

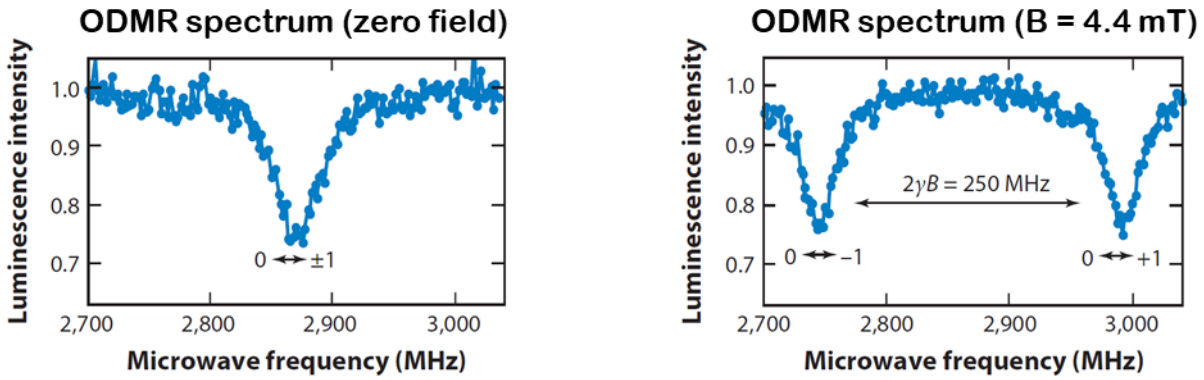

Figure 2.10: ODMR spectra of a single NV centrum. Picture adopted from.[76]

The ODMR can be performed in continuous or pulsed mode for the laser and the MW excitation. The **continuous-wave (CW)** experiment is the most direct approach but on the other hand, it is more suitable especially for less sensitive measurements and mainly, it can be not use for measuring spin dynamics. In the CW experiment, green laser illumination, as well as MW excitation is applied continuously (see *Figure 2.11)*. With this arrangement, it is possible to determine the magnitude the magnetic fields by the separation of the two peaks, which is linearly dependent on the B field magnitude.

The second approach is the pulse experiments, which are more sensitive than the continuous-wave experiments and allow for various detection schemes (such as detection of AC fields or nuclear magnetic resonance techniques). The laser and MW excitations are pulsed in these experiments and are switched off during the sensing period.

A very interesting type of pulse experiment is ***T*$_1$ relaxation time** measuring. After polarization to either $m_s = 0$ state (or $m_s = \pm 1$ state with the use of microwave), the electrons tend to fall back to thermally mixed state (superposition of the two states). The average time required for the transition from the polarized state to the mixed state is called the spin-lattice relaxation time (T_1 relaxation time). The T_1 relaxation time is a few milliseconds for bulk diamond at room temperature[88] while for the nanoparticles, the T_1 relaxation time is shortened to tens of microseconds.[61]

T_1 relaxation measurements can be performed with or without microwave radiation. Experiments without the use of microwave radiation are a huge advantage, especially when it comes to detection in living systems, because they avoid the thermal effects and other interferences that microwave radiation causes.

The pulse sequence is similar for both cases (see *Figure 2.11)*. Initially, electrons are introduced to spin sublevel $m_s = 0$ of the ground state by the means of an initiating laser pulse. Subsequently, in the case of relaxometry using microwave radiation, a microwave π pulse is applied, which changes the spin state of the electrons to the sublevels $m_s = \pm 1$. In the absence of a microwave pulse, electrons remain in the spin sublevel $m_s = 0$. The whole system is allowed to develop for a certain time (dark time τ) after which the resulting spin state is read by the means of a second laser pulse (detection pulse).

The T_1 relaxation is the measured point-by-point by prolonging the dark time τ and repeating the whole sequence multiple times. In the case of relaxometry using microwave radiation, the graph of the dependence of fluorescence on the dark time is an increasing exponential function. When it comes to relaxometry without the use of microwave radiation, this exponential is decreasing.[89] After fitting these functions, the T_1 relaxation time is obtained as a constant of the mono-exponential fit.

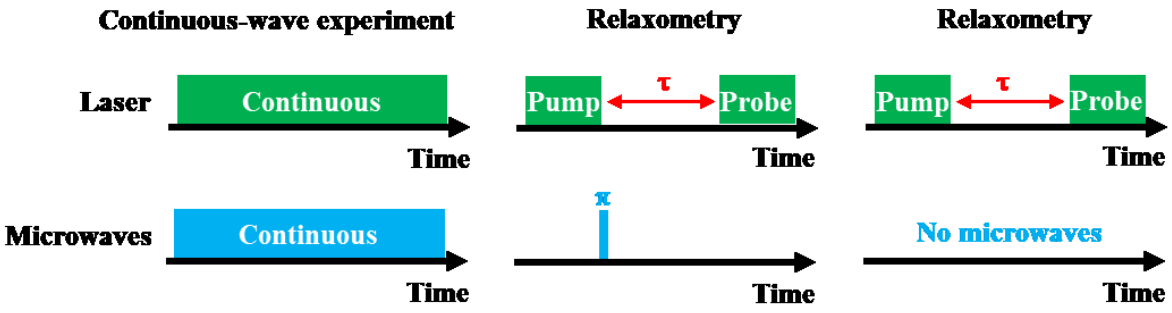

Figure 2.11: Time depiction schemes of individual ODMR experiments

Based on the T_1 relaxation time value, it is possible to determine concentration of paramagnetic species in the close proximity of the NV centre.[90] For instance, the dependence of the T_1 relaxation time on the concentration of paramagnetic ions in the vicinity of the FNDs coupled with appropriate chemistry could be potentially used for quantum sensing in living cells. By monitoring the T_1 relaxation change, the concentration or even the distance of the probed species can be, in principle, determined. For instance, decrease of T_1 means an increase of the probed ions concentration or, alternatively, decrease in its distance to the FND.

Once of the paramagnetic ions that can be detected are Gd^{3+} ions. Free Gd^{3+} ions are toxic and, in order to be useful in influencing the T_1 relaxation time, their complexation is necessary. Most often, Gd^{3+} ions are complexed into macrocyclic ligands. These complexes are characterized by significant thermodynamic stability and kinetic inertness and therefore their toxicity is minimal.[91]

The use of Gd^{3+} ions for quantum sensing application is not surprising because no other ion has seven unpaired electrons in valence orbitals. However, there are two ions – dysprosium(III) and holmium(III), which have a higher magnetic moment than Gd^{3+} (due to the orbital contribution to the electron angular momentum). The main reason why Gd^{3+} ions are used is due to symmetry, which causes a much slower relaxation compared to asymmetrically arranged spins of dysprosium(III) and holmium(III) ions.[92]

Surface modification of nanodiamonds is required to attach the paramagnetic ion of gadolinium or other chemical particles useful in quantum sensing. The surface modifications of FNDs thus constitute a major part in the development of selective and sensitive probes.

2.4.4 Direct surface modifications

In general, the reactivity of NDs is affected by their size and shape. The smaller the NDs, the more reactive they are, and the most reactive shapes include a spherical shape. The third important property influencing reactivity is the amount of sp^2 carbon atoms on the NDs surface.

The type and the amount of the functional groups on the NDs surface depends on the NDs preparation methods. In most cases, we obtain an oxygenated surface of nanodiamonds. This is due to the use of water or ice as a cooling medium after the detonation process (DNDs and HPHT NDs), which leads to the formation of hydroxyl groups. In addition, one of the most common post-synthetic treatments of NDs is the oxidative treatment using oxidizing mineral acids, which, as the name implies, also leads to the formation of carbonyl and carboxyl groups on the NDs surface.[77] On the other hand, CVD NDs have their surface covered mainly with hydrogen atoms, which is a consequence of the use of hydrogen gas in their synthesis.[93] However, even this type of NDs is treated, as was the case with DNDs and HPHT NDs, which again leads to an oxygenated surface.[94]

As was mentioned above, the main functional groups on the nanodiamonds surface are carboxyls, carbonyls, various functionalized alcohols, ethers, lactones and esters (see *Figure*

2.12 – **black colour**).[95] Depending on the representation and termination of these groups, zeta potential varies from –50 mV to +50 mV.

The carboxyl group, which represents the maximally oxidized state, is one of the most common groups on the NDs surface. Harsh oxidation is carried out with a mixture of strong oxidizing mineral acids (see *Figure 2.12* – **light blue colour**). The most common is equimolar mixture of concentrated hydrochloric acid (HCl), nitric acid (HNO_3) and sulphuric acid (H_2SO_4).[77] It is also possible to use a mixture of sulphuric acid (H_2SO_4) and hydrogen peroxide (H_2O_2) or a mixture of concentrated nitric acid and sulphuric acid in the volume ratio of a 1:3.

Such an oxidative treatment is logically associated with the weight loss of nanodiamonds (removal of non-diamond carbons) and thus also with a reduction in the size of NDs.[96] It is important to note that disordered sp^2 carbons are much more reactive than diamond carbons.[77] The oxidation therefore results not only in the introduction of oxygenated groups on the NDs surface but also in the achievement of the nanodiamonds phase purity.

Another way to achieve an oxygenated surface of NDs is by air oxidation. Gogotsi et al. described the controlled air oxidation at various temperatures.[97] They found that the choice of temperature is crucial to achieve the desired oxidation. The temperature must not be too low, as there will be no quantitative oxidation but also not too high, because there will be a large size reduction of the nanodiamond. This way, the majority of surface groups on the NDs are carboxyl groups, which carbonyl, alcohol and ether groups accompany.

Nanodiamonds subjected to oxidative treatment, whether with acids or air, are typically hydrophilic and can be dispersed in polar solvents. Typically, they have zeta potentials from –30 to –50 mV.

Another very useful functional group, which can be directly attached to the surface of NDs, is the hydroxy group. Hydroxy-functionalized nanodiamonds offer a wide variety of subsequent reaction.

There are several approaches to prepare nanodiamonds coated with a sufficient number of -OH groups (see *Figure 2.12* – **dark green colour**). One of the most straightforward approach is the use of borane (BH_3) to reduce the carbonyl groups already presented to hydroxy groups.[98] However, ester and lactone groups remain intact and therefore this method is limited to those types of nanodiamonds, which contain mainly carbonyl and carboxyl groups on their surface. On the other hand, the use of borane followed by the acid treatment causes removal of sp^2

carbon atoms (addition of water to the double bond) and introduction of hydrogen atoms on the nanodiamonds surface.

In order to reduce all functional groups to alcohol groups, it is necessary to use a stronger reducing agent, such as $LiAlH_4$. However, this reducing agent does not remove the present sp^2 hybridized carbon atoms.[99]

Another way to directly introduce OH groups to the NDs surface is using a so-called Fenton's reagent.[100] The Fenton's reagent is a mixture of ferrous sulphate ($FeSO_4$) and hydrogen peroxide (H_2O_2). Its advantage is that the hydroxy groups are formed in situ. It is also an oxidizing agent and therefore removes all non-diamond carbon.

Regardless of the used method, OH-functionalized NDs show a zeta potential about +40 mV and can be dispersed in polar solvents.

As was mentioned, the surface of nanodiamonds is naturally covered by various oxygen groups. Hydrogenation of such nanodiamonds is particularly difficult because use of most reducing agents does not lead to complete reduction (complete removal of functional groups) but to the formation of hydroxyl groups.

In organic chemistry, the hydrogenation is typically performed using hydrogen gas in a presence of a metal catalyst such as palladium, platinum or nickel, but this method has not been applied to the hydrogenation of nanodiamonds. The explanation is, that it is very difficult to remove the used metal catalyst quantitatively, because it is not possible to oxidatively decompose the catalyst, without simultaneous oxidation of the nanodiamonds.

One of the few published approaches for direct hydrogenation uses hydrogen gas at suitable high temperatures (see *Figure 2.12* – **gold colour**).[101]

Another very important functional group is an amino group. The chemistry of the NH_2 group is well known and therefore its introduction opens up a large number of pathways for further functionalization of the NDs. For example, it allows the attachment of various bioactive polymers by amidation, reductive amination or direct condensation.

However, the direct introduction of the NH_2 groups on the NDs surface is very difficult. One published approach uses the reaction of chlorinated nanodiamonds with gaseous ammonia at appropriate temperatures (see *Figure 2.12* – **dark red colour**).[102] Other approaches introduce the NH_2 groups on the NDs surface, too, but the amino groups are connected via linkers. They

involve the use of the amidated silanes[98] or a multi-step method based on the hydroxylated nanodiamonds.[103]

In addition to the functional groups already mentioned, there are other, less common functional groups that can be attached directly to the NDs surface. For instance fluorine can be introduced by a reaction with gaseous mixture of fluorine and hydrogen at suitable temperatures (see *Figure 2.12* – **brown colour**).[104] In contrast, the photochemical reaction of gaseous chlorine with hydrogenated nanodiamonds is used to introduce chlorine to the surface of NDs (see *Figure 2.12* – **pink colour**).[102] Bromine is even less common. The wet-chemical reaction of hydroxylated NDs with N-bromosuccidimide (NBS) in carbon tetrachloride (CCl_4) is most commonly used for the partial bromination of the NDs (see *Figure 2.12* – **light green colour**).[100] However, halogenated nanodiamonds are not stable enough and readily react with atmospheric moisture to form halohydrines.

A very rarely used functional group that can be introduced on the NDs surface is a thiol group. It can be attached directly on the surface of NDs by a photochemical reaction of molecular sulphur (see *Figure 2.12* – **purple colour**).[105]

Last, an azide group can be used as a direct surface modification (see *Figure 2.12* – **dark blue colour**). This group has found large application in recent years in so-called click chemistry (azide-alkyne click). This approach is based on carboxylated NDs, which undergo silver-catalysed (AgF) decarboxylation to give fluorinated NDs. However, fluorine atoms are immediately substituted in situ for azide groups from tosylazide (TsN_3). The advantages of this reaction is that it takes place in aqueous solutions under mild conditions with commercially available reagents.[106]

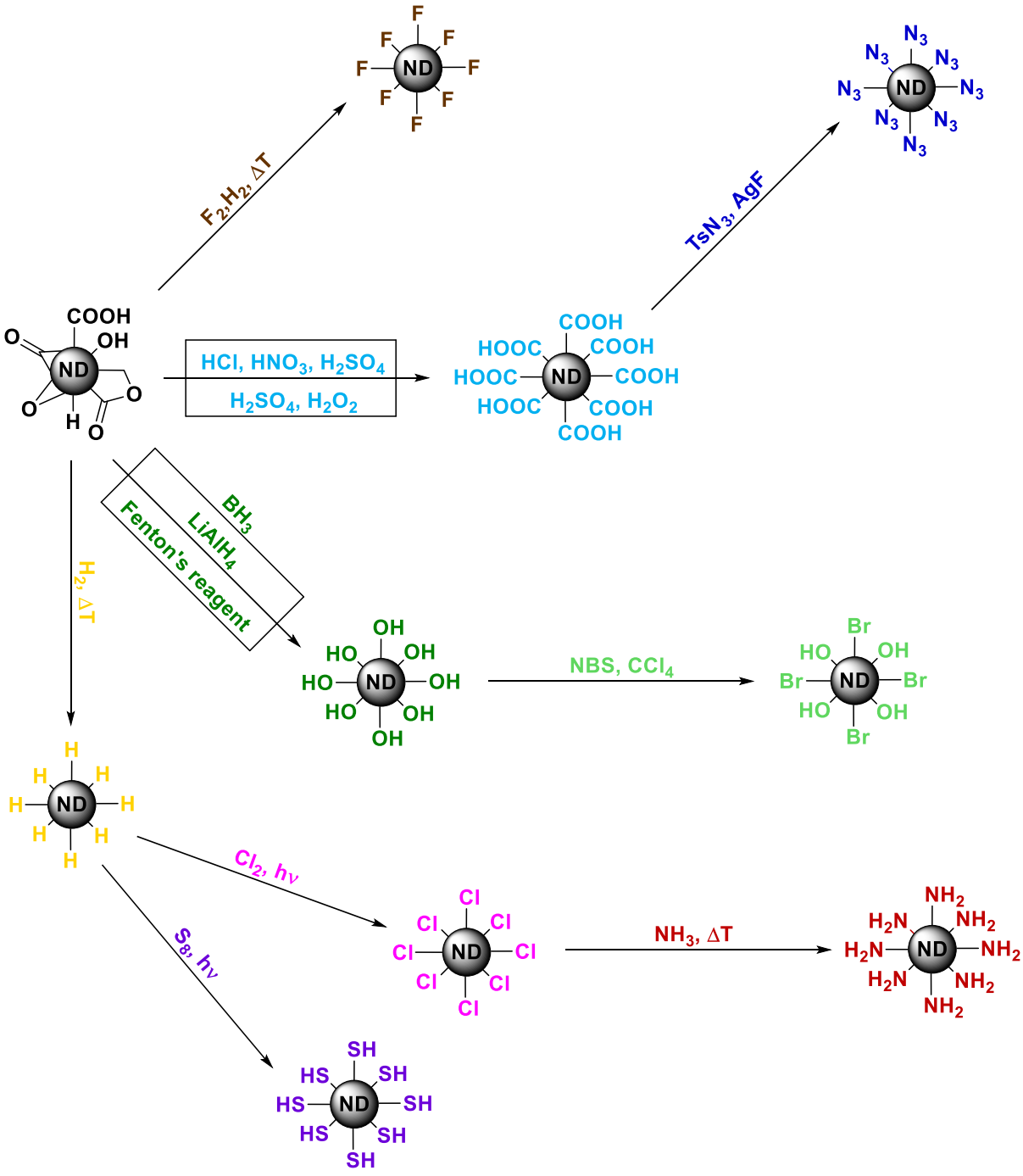

Figure 2.12: Direct surface modification of NDs

3. Aims of the work

The main goal of this work is to design and develop selective probes for miRNA detection with a potential for localized intracellular sensing. The aim is to functionalize fluorescent nanodiamonds with transducers that would allow selective binding of the specific miRNA and its consequent detection. For this purpose, an approach based on molecular beacons modified with gadolinium paramagnetic ions (Gd^{3+}) had to be developed and covalently attached to the FND surface. Furthermore, the optimal conditions for the construction of such a detection system had to be found.

The main objectives of this work can be divided into following subtasks:

(i) To design the molecular beacon sequence that would allow detection of the target molecule as well as its end modification with Gd^{3+} and subsequent attachment to the FND surface.

(ii) To covalently attach the complex containing Gd^{3+} ion to one end of the molecular beacon and a chain containing DBCO molecule to the other end of the molecular beacon to facilitate attachment of MBs to FNDs.

(iii) To modify the surface of fluorescent nanodiamonds with azide groups and to attach subsequent the modified molecular beacons.

(iv) To characterize the entire detection system by measuring the T_1 relaxation time without and with the target molecules present in the solution.

4. Experimental part

4.1 Material and methods

4.1.1 General information

All chemicals and solvents were supplied by Sigma-Aldrich, Qiagen, Alfa Aesar, Acros Organics, Penta, Lach-Ner or VWR. They were used without subsequent purification, unless the purification step is emphasized in the Synthetic part. When working with nanodiamonds, MilliQ water, HPLC methanol, HPLC acetonitrile were used. When DMSO is mentioned, dry DMSO was used.

All DNA or RNA sequences were purchased from IDT (Integrated DNA Technologies, Inc.) with HPLC purification as a lyophilizate.

Temperature of the reactions was monitored directly in aluminium block using a temperature sensor.

4.1.2 List of instruments and used software

Following instruments were used in this work:

- Centrifuge: Eppendorf centrifuge 5430
- Lyophilisation: Labconco CentriVap Cold Trap
- Sonicator bath: Ultrasonic Cleaner Elmasonic PH350EL
- Spectrometer: Tecan Multimode plate reader Spark, Software 2.3
- RNA box: Biosafety Cabinet BSC-7001 1-1
- DLS: Zetasizer Nano ZS, Software version 7.13
- Nanodrop: NanoDrop One, Thermo Scientific™
- LC-MS: Agilent 6230 TOF LC/MS
- ICP-MS/MS: Agilent 8900 with SPS 4 autosampler and ISIS3 sample introduction system
- T_1 time: home-built confocal fluorescence microscope

We also used following simulation program during our work:

- OligoAnalyzer™ Tool from IDT

4.1.3 Fluorescence measurements

Fluorescence measurements, except for the T_1 relaxation time measurement, were performed on Tecan Spark. In all cases, Thermo Scientific™ Nunc 384-Well Optical Bottom Plate was used for the measurements of the MBs in solution. The volume of each sample was 25 µl per well and all measurements were performed at 37 °C in triplicates, if not mentioned otherwise.

For the fluorescence measurements of nanodiamond colloidal solutions, Thermo Scientific™ Nunc MicroWell 96-Well Optical-Bottom Plate was used. The volume of each sample was 100 µl per well and all measurements were performed at 25 °C in triplicates, if not mentioned otherwise.

4.1.4 Dynamic light scattering

Dynamic light scattering was used for determination of hydrodynamic diameter of nanodiamonds. For measurements, 100 µl of FND aqueous colloidal solution of approximately 0.1 mg/ml concentration was used. All measurements were performed in quartz cuvettes at 25 °C with equilibration time of 30 s. Hydrodynamic diameters are given in nm, rounded to three significant figures.

4.1.5 LC-MS spectrometry

Liquid chromatography coupled with a mass detector (LC-MS) was used to determine the purity and degree of conversion of the MB end modifications. LC-MS measurement were performed on Agilent 6230 TOF LC/MS on Agilent column (Agilent Eclipse Plus C18, 1.8 um, 2.1x50mm). In the chromatography method, solvent A was H_2O + 0.1% ammonium acetate and solvent B was acetonitrile (ACN). The elution began with 0 % of solvent B and continued with gradient to 30 % of solvent B (6.0 min). Peaks were detected using UV 260 nm detector coupled with ESI source of ionization (ESI-MS). 18 µl of a solution of MB in water with an approximate concentration of 10 µM was used for each analysis. Results were processed using Agilent Mass Hunter.

4.1.6 ICP mass spectrometry

Determination of gadolinium content attached to fluorescent nanodiamonds modified via molecular beacons (FND-DBCO-DNA-Gd) was carried out by inductively coupled plasma mass spectrometry with triple quadruple (ICP-MS/MS) using Agilent 8900 spectrometer with SPS 4 autosampler and ISIS3 sample introduction system. Gadolinium was detected at m/z $156 \rightarrow 172$, $157 \rightarrow 172$ and $158 \rightarrow 173$ in MS/MS O_2 reaction mode with mass shift (O_2 40% gas flow rate) to assure interference free analysis. Quantification was performed using five-point external calibration (0.5 – 4.0 $\mu g \cdot l^{-1}$ Gd). Calibration standards were prepared from a 1000 $mg \cdot l^{-1}$ Gd stock standard solution in 0.2% (m/v) HNO_3 (Honeywell, semiconductor grade). Results were processed using Agilent Mass Hunter and are means of 3 parallel ICP-MS/MS measurements at 3 m/z.

4.1.7 T_1 measurements

The T_1 relaxation time of the NV centres in the fluorescent nanodiamonds was measured using a home-built confocal fluorescence microscope. The NV centres were excited using a series of ~ 10 μs long 532 nm laser (25 μW measured before the objective), which was focused onto the sample using an oil-immersion objective (Olympus UPlanSApo 60x oil, N.A. = 1.35). The resulting fluorescence from the NV centres is collected by the same objective and filtered with a 650 nm long-pass filter and detected using an avalanche photodiode.

The measurement of T_1 relaxation time was carried out by Priya Balasubramanian and Maabur Sow in the laboratory of Dr. Fedor Jelezko at the University of Ulm.

4.2 End modifications of MB

4.2.1 Preparation of Gd-MB

5.0 µl (5 nmol; 1000 µM) of MB solution was pipetted into a 0.5ml Eppendorf tube. Subsequently, 2.5 µl (10 000 µM) of a solution of the complex containing gadolinium in DMSO was added by pipette. In the second Eppendorf tube, 2.0 µl (100 mM) of BTTP solution in DMSO was mixed with 5.0 µl (20 mM) of $CuSO_4$ solution in water. From this solution, 3.5 µl was added to the reaction mixture in the first Eppendorf tube. Then, 1.25 µl (100 mM) of aminoguadinine hydrochloride solution in water and 5.0 µl (pH = 7.0; 500 mM) of HEPES solution in water were added to the reaction mixture to keep a constant pH during the reaction. After that, 4.0 µl of DMSO was added making final concentration of DMSO in the reaction mixture to be 30 weight percent. Finally, 4.0 µl (100 mM) of freshly prepared sodium ascorbate solution in water was added. The whole reaction mixture was first stirred with a pipette and then stirred at RT for 3 h. After the 3 h, the reaction mixture was diluted by the addition of 450 µl H_2O. The solution was quantitatively transferred to an AMICON filter (3 kDa) and centrifuged (14 000 g; 20 min; 4 °C). The filtrate was removed, the pellets on the filter were resuspended in water and centrifuged again under the same conditions. The whole process was repeated for the total number of six washing steps. As a result, 2.95 nmol of a solution of Gd-MB in water was obtained, representing a yield of 59 %. The solution was stored in a freezer at –20 °C.

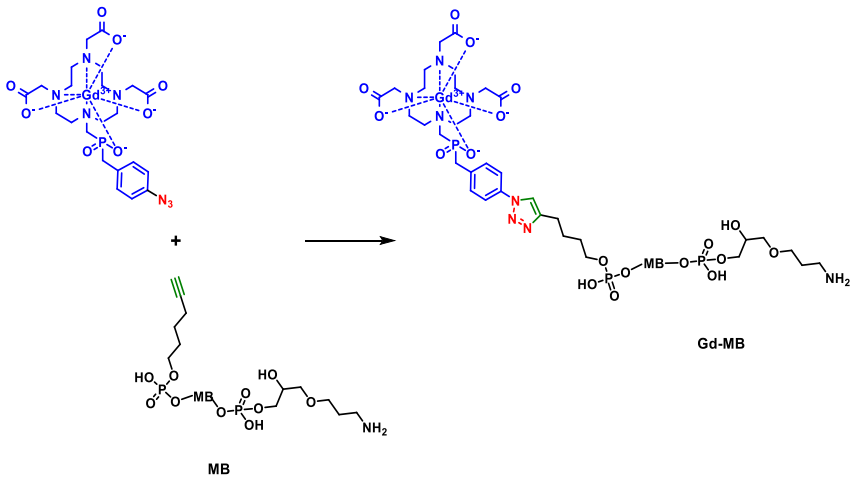

Figure 4.1: Synthesis of Gd-MB

4.2.2 Preparation of Gd-MB-DBCO

9.51 µl (5 nmol; 33.04 µM) of Gd-MB solution was pipetted into a 0.5ml Eppendorf tube. 7 µl of DMSO was added to the reaction mixture. Subsequently, 2.5 µl (250 nmol; 20 mM) of a DBCO-PEG$_4$-NHS ester solution in DMSO was added by pipette. Then, 1.0 µl (pH = 7.4; 500 mM) of HEPES solution in water were added to keep a constant pH during the reaction. The whole reaction mixture was stirred at RT for 1.5 h. After the 1.5 h, the reaction mixture was diluted by adding water so that the total volume was 500 µl. The solution was quantitatively transferred to an AMICON filter (3 kDa) and centrifuged (14 000 g; 20 min; 4 °C). The filtrate was removed, the pellets on the filter were resuspended in water and centrifuged again under the same conditions. The whole process was repeated for the total number of seven washing steps. The solution of Gd-MB-DBCO in water was lyophilized obtaining 2.97 nmol of Gd-MB-DBCO, which represented a yield of 59 %. The product was stored in a freezer at –20 °C.

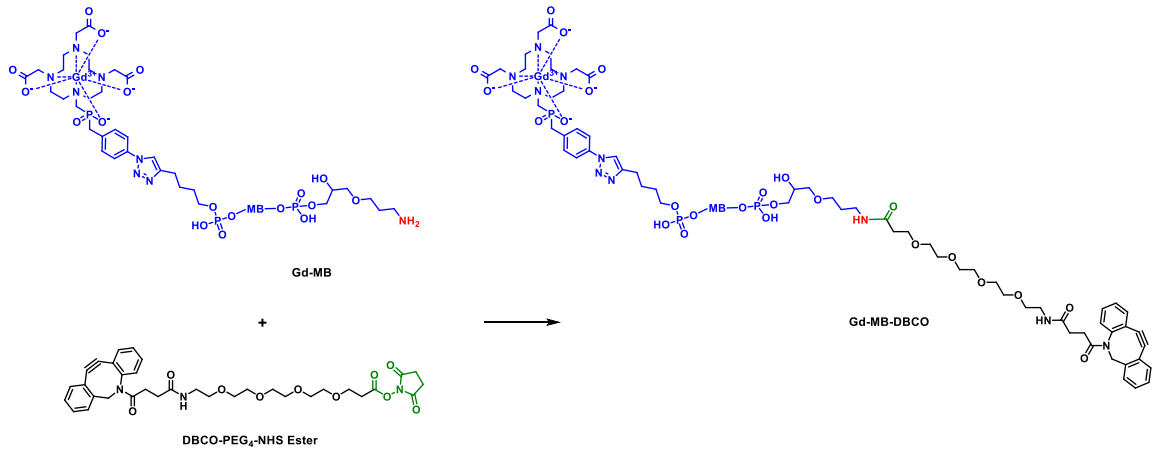

Figure 4.2: Synthesis of Gd-MB-DBCO

4.3 Preparation of fluorescent nanodiamonds coated with molecular beacons

4.3.1 Oxidization of NDs

HPHT NDs (1.3 g) were grounded thoroughly in agate mortar with pestle and then oxidized by air in a tube furnace for 6 h at 550 °C. The NDs (1.12 g) were then transferred to a Teflon container and mixture of concentrated HNO_3 and HF (1:2 v/v) was added. The total volume of the acid mixture was 30 ml. The mixture was heated to 160 °C and stirred for 48 h. The black

ND suspension was quantitatively transferred to two Falcon tubes, diluted with water to a total volume of 24 ml in each tube and centrifuged (20 000 g; 20 min; 20 °C). Supernatant was removed and the pellets were suspended in a water and centrifuged again at the same conditions. This washing step was then repeated with 1M NaOH solution, water, 1M HCl solution and finally 3 times with water. After all centrifugation steps, the colloidal solution was transferred to a 100ml flask and lyophilized, providing dark ND powder. The average particle size was determined by DLS to be ~ 50 nm from intensity distribution.

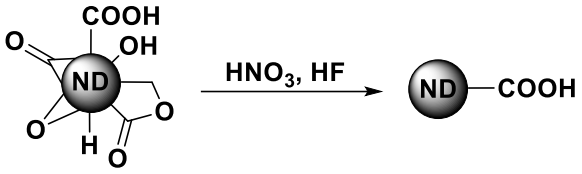

Figure 4.3: Oxidization of NDs

4.3.2 Preparation of FNDs

Fluorescent nanodiamonds (FNDs) were prepared from the purified ND powder described above. 1.0 g of the purified ND powder was placed on thick aluminium target and irradiated with electron beam. The irradiated material was annealed for 1 h at 900 °C and then oxidized by air in a tube furnace for 4 h at 450 °C. Then the air oxidized FNDs were transferred to a Teflon container and treated with 30 ml of mixture of concentrated H_2SO_4, $HClO_4$ and HNO_3 and (1:1:1, v/v/v). The mixture was heated to 90 °C and stirred for 48 h. After cooling to RT, the suspension of FNDs was quantitatively transferred to two Falcon tubes, diluted with water to a total volume of 24 ml in each tube and centrifuged (20 000 g; 20 min; 20 °C). Supernatant was removed and the pellets were suspended in a water and centrifuged again at the same conditions. This washing step was then repeated with 1M NaOH solution, water, 1M HCl solution and finally 3 times with water. After all centrifugations, the colloidal solution was transferred to a 100ml flask and lyophilized, providing 0.675 g of black FND.

4.3.3 Preparation of FND-N_3

20 mg of FNDs were mixed with 1.0 ml of water in a 1.5ml Eppendorf tube and the mixture was sonicated for 30 min in a cup horn sonication (pulse on: 1 s; pulse off: 1 s). The colloidal solution of FND was quantitatively transferred to a 4ml vial and 1.0 ml of ACN was added. In the meantime, 6.0 mg (0.047 mmol) of AgF was dissolved in 0.1 ml of water in a 0.5 ml

Eppendorf tube and 26 mg (0.096 mmol) of $K_2S_2O_8$ was dissolved in 0.1 ml of water in another 0.5ml Eppendorf tube. The solution of AgF, solution of $K_2S_2O_8$ and 20 µl (26 mg; 0.130 mmol) of TsN_3 were added to the FND colloidal solution while stirring continuously. The reaction vessel was purged with argon and the reaction mixture stirred for 18 h at 50 °C under argon atmosphere. After cooling to RT, the solution was divided into twelve Eppendorf tubes and centrifuged (30 000 g; 30 min; 20 °C). Supernatant was removed and the pellets were suspended in a water and centrifuged again 30 000 g; 30 min; 20 °C). Following the same conditions, the sample was further washed two times with water, two times with ACN and again two times with water. After last centrifugation, the sample was diluted in 2.0 ml of water providing concentration 8.5 mg/ml of FND-N_3 in water and stored in a fridge at 4 °C. The final amount of FNDs were determined gravimetrically. This procedure was designed according to the published work.[106]

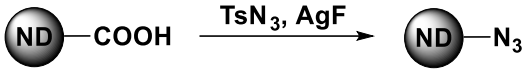

Figure 4.4: Preparation of FND-N_3

4.3.4 Preparation of FND-DBCO-MB-Gd

500 µg of FND-N_3 was quantitatively transferred to 1.5ml Eppendorf tube and centrifuged (50 000 g; 40 min; 20 °C). Supernatant was removed and the pellet was suspended in a 100 µl of dry DMSO. Very gentle sonication in a sonication bath is required to prevent aggregation of the particles. 50 µl (2.325 nmol) of DBCO-MB-Gd in DMSO was added to the reaction mixture. The reaction mixture was frozen by immersion in liquid nitrogen for 5 min. Subsequently, the mixture was melted in warm water. These freeze-and-thaw cycles were repeated ten times totally, and after every third cycle, the reaction mixture was gently sonicated. A small amount of a 1M solution of NaI in DMSO was added to the reaction mixture to obtain a final concentration of 25 mM NaI in the reaction mixture. Freeze-and-thaw cycle was repeated five times. Again, a small amount of a 1M solution of NaI in DMSO was added to the reaction mixture to obtain a final concentration of 50 mM NaI in the reaction mixture and freeze-and-thaw cycle was repeated three times. Then, a small amount of a 1M solution of NaI in DMSO was added to the reaction mixture to increase a final concentration to 100 mM NaI in the reaction mixture and freeze-and-thaw cycle was repeated three times. Finally, a small amount of a 1M solution of NaI in DMSO was added to the reaction mixture to reach a final concentration of 200 mM NaI in the reaction mixture. After aggregation of particles, the total

volume of the mixture was adjusted to approximately 1 ml with adding of DMSO. The reaction mixture was placed in preheated water bath (70 °C) and left there for 5 min. Immediately, the Eppendorf tube was centrifuged (50 000 g; 30 min; 40 °C) in a preheated rotor (10 min in an oven set at 120 °C). Supernatant was removed and the pellets were suspended in fresh DMSO. The whole washing procedure was repeated 4 times with DMSO and then 5 times with water. After last centrifugation, the sample was transferred to 0.5 ml of water providing concentration 1.0 mg/ml of FND-DBCO-MB-Gd in water and stored in a fridge at 4 °C.

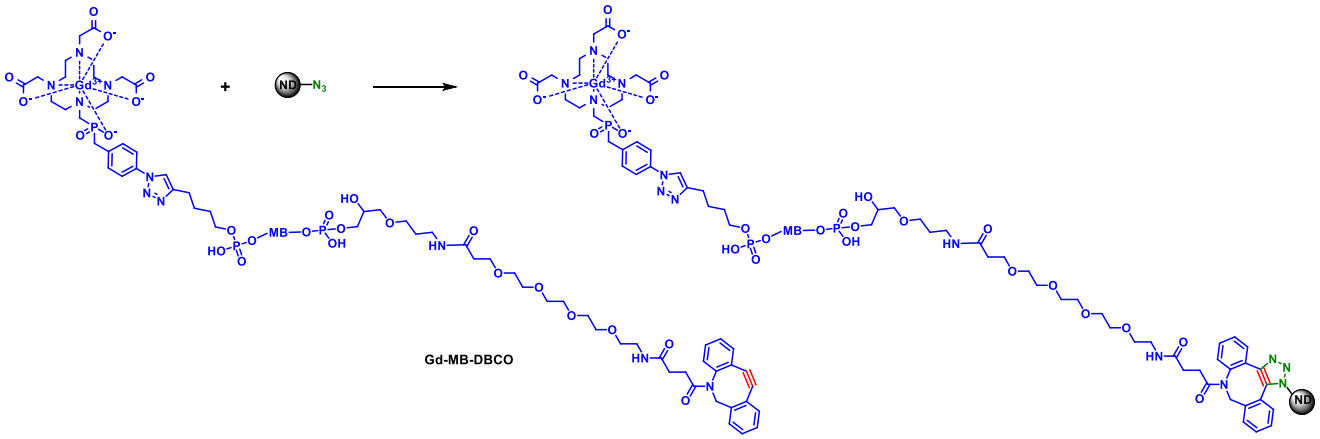

Figure 4.4: Synthesis of FND-DBCO-MB-Gd

5. Results

5.1 The basic principle of the detection system design

We designed a detection system based on the use of Gd^{3+} modified molecular beacons, which are covalently attached to the surface of fluorescent nanodiamonds. The principle of detecting the target hsa-miR-19a-3p molecule (miRNA molecule) takes advantage of the fact that the molecular beacons are closed in the absence of the target molecule, whereas in the presence of miR-19a-3p molecule the MB opens up due to the hybridization of the loop. Commonly, a fluorophore and a quencher molecule are used to detect hybridization. In our design, however, we attached a complex containing a Gd^{3+} ion to the 5' end of the MB and the other end is bound to the FND (see *Figure 5.1*). Due to strong magnetic environment of the Gd^{3+} 7/2 spin, the T_1 relaxation time is short, when the MB is in the closed state and the Gd^{3+} ions are close to the surface of the FNDs. After hybridization with the miR-19a-3p miRNA molecule, the MB opens up moving the Gd^{3+} ions further from the FNDs. This change results in a significant increase in T_1 relaxation time and allows to detect the presence of a target miRNA molecule based on the relaxometry measurements.

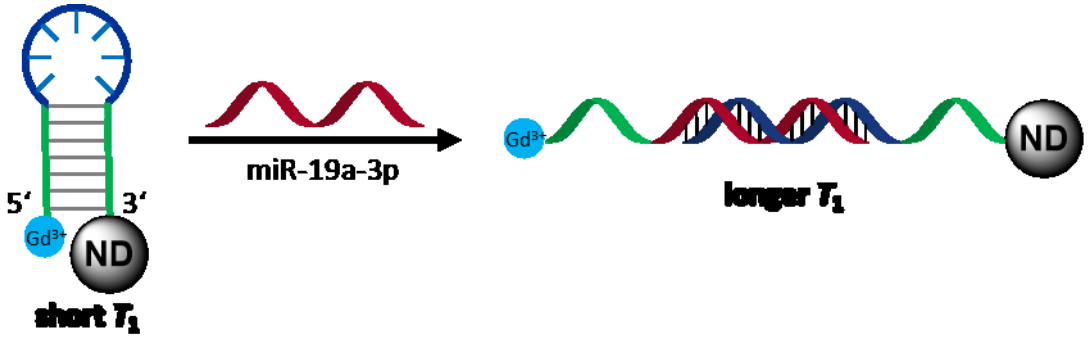

Figure 5.1: Basic principle of our detection system

5.2 Preparation strategy of the whole detection system

Figure 5.2 shows the strategy for preparing the entire detection system. In order to make the sensing of miRNA as sensitive as possible, it is necessary that the Gd^{3+} ions in the closed MB conformation are as close as possible to the FND surface and thus as close as possible to the NV centres. Conversely, in the open state, they need to move as far as possible from FNDs to make the change in T_1 relaxation time most considerable.[61] For this reason, it is ideal to attach

the whole MB directly by modifying the crystal lattice of the fluorescent nanodiamonds. The gadolinium-containing complex contains an azide group. Therefore, we modified the 5' end of the MB by alkyne group to attach the gadolinium complex using an azide-alkyne click. We modified the 3' end of the MB with an NH_2 group because this group reacts well with the NHS ester of DBCO to form an amide bond. The DBCO group is suitable for another azide-alkyne click. For this purpose, the FND surface was directly modified with azide groups (see *part 4.3.3* for details on the preparation).

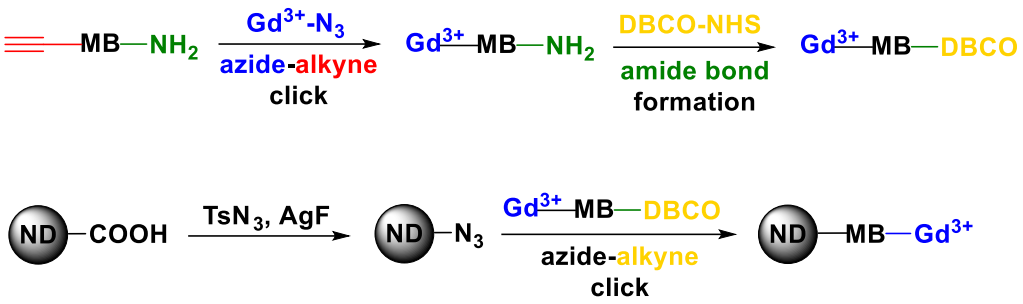

Figure 5.2: A schematic strategy of the preparation of the whole detection system

5.3 Molecular beacon design for a quantum sensing application

The right molecular beacon design is the key factor in using the entire system to detect a target miRNA molecule. The loop sequence is given by the sequence of the detected miRNA molecule, because it has to be complementary to the miRNA. Therefore, the optimization process consists mostly of the selection of the stem sequence. Important parameters are the length of the stem, the order of complementary nucleotides in the stem, and the possible insertion of one or two nucleotides, that form neither the stem nor the loop, to increase the preference for ideal molecular beacon formation (reducing the formation of the other secondary structures, containing smaller loops).

5.3.1 A structure prediction using a computer program

The design of the entire MB consisted of several steps. The first and the easiest step was to create a loop sequence based on the complementarity of the nucleotides to the detected miR-19a-3p miRNA molecule. In the second step, we tested different lengths of stems from four pairs of mutually complementary nucleotides to seven pairs. The optimal stem length was

five nucleotide pairs, because the melting temperature (T_m) of longer stems was too high, while four-nucleotide pair MBs were unstable and formed too many different secondary structures.

Subsequently, we tested different contents of GC pairs in the stem. Four GC pairs proved to be the best, because these stems had a T_m higher than 40 °C. This is essential for use in the living cells, as MB needs to be closed at 37 °C. Stems with three or less GC pairs had the T_m too low, while stems with five GC pairs, too high.

The next step in the optimization process was the position of the AT pair. We found out that the position of the AT pair affects the preference for the formation of different secondary structures, but we did not observe any dependence that could be generalized.

Since even after all these optimization steps, we did not reach the structure of the ideal MB (MB with only one loop), we decided to insert between the stem and the loop nucleotide or nucleotides. We explored the effect of inserting one or two nucleotides on one or the other side of the stem, such as inserting a pair of nucleotides that were not complementary to each other. It is the insertion of such a nucleotide that has helped to increase significantly the probability of creating an ideal MB.

We analysed more than 100 proposed MBs designs using a computer program and selected the three best ones (N°2, N°3, N°5). As can be seen in the *Table 5.1*, the individual sequences differ only in the presence and type of non-complementary nucleotides between the stem and the loop, but even such a minimal change has a huge impact on possible secondary structures.

Table 5.1: The sequence of the probed miRNA molecule and the sequences of three promising molecular beacons. The blue colour indicates the loop sequence, the black colour represents the mutually complementary sequences of the stem and the red colour highlights the nucleotides that do not form either a stem or a loop.

Label	Sequence (5'–3')
miR-19a-3p	UGU GCA AAU CUA UGC AAA ACU GA
MB N°2	**CGC TC T TCA GTT TTG CAT AGA TTT GCA CA T GA GCG**
MB N°3	**CGC TC C TCA GTT TTG CAT AGA TTT GCA CA T GA GCG**
MB N°5	**CGC TC TCA GTT TTG CAT AGA TTT GCA CA T GA GCG**

The individual parameters of these three promising MB designs were calculated using the computer program (OligoAnalyzer^{TM} Tool from IDT) and their possible secondary structures were characterized. These resulting parameters are summarized in the *Table 5.2*. and the possible secondary structures are displayed in *Figure 5.3*.

Table 5.2: The parameters characterizing probable secondary structures of the individual MBs where ΔG stands for Gibbs energy, ΔH for enthalpy, ΔS for entropy and T_m for melting temperature

MB N°2				
Structure	ΔG (kcal/mol)	T_m (°C)	ΔH (kcal/mol)	ΔS (cal/K·mol)
A1	–5.09	47.6	–72.1	–224.8
A2	–4.12	43.7	–69.9	–220.6
A3	–3.62	40.9	–71.4	–227.4
A4	–2.70	37.3	–68.0	–219.0
MB N°3				
Structure	ΔG (kcal/mol)	T_m (°C)	ΔH (kcal/mol)	ΔS (cal/K·mol)
B1	–2.10	42.1	–38.8	–123.1
B2	–1.90	33.4	–69.2	–225.7
B3	–1.23	30.4	–69.9	–230.3
B4	–1.09	30.3	–62.2	–205.0
MB N°5				
Structure	ΔG (kcal/mol)	T_m (°C)	ΔH (kcal/mol)	ΔS (cal/K·mol)
C1	–5.33	48.8	–72.1	–223.9
C2	–4.67	45.9	–71.5	–224.1
C3	–4.27	44.4	–69.9	–220.1

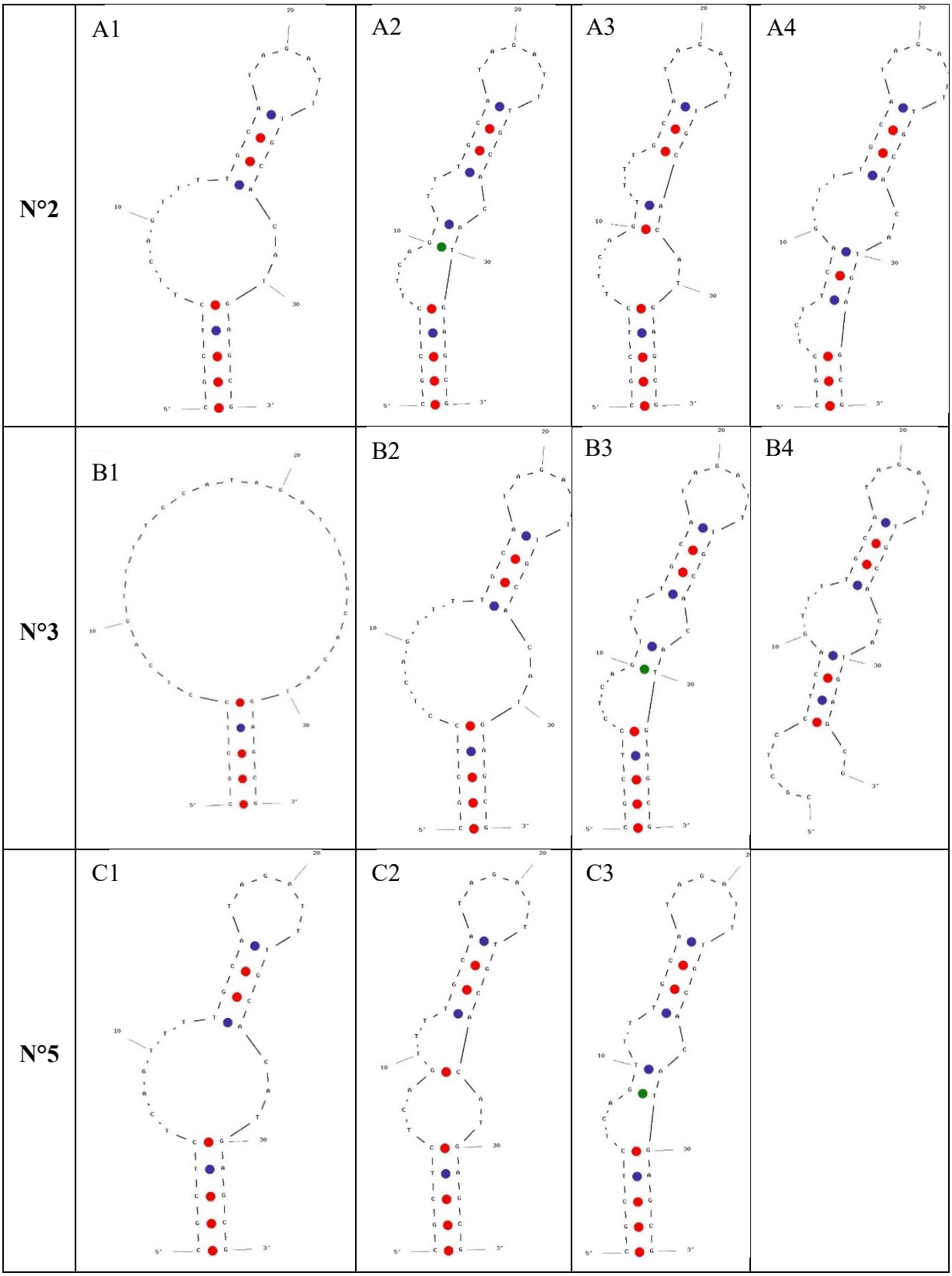

Figure 5.3: Secondary structures of the individual MBs arranged in descending order of a stability from left to right.

Out of the three selected designs, the MB N°3 was the only one with the structure of an ideal molecular beacon (see *Figure 5.3* – B1), while the remaining two had the most probable secondary structure composed of two smaller loops. It should be noted that the MB N°3 showed the highest T_m difference between the two most probable structures, which means that it preferentially exists in a single-loop conformation at 37 °C. On the other hand, the difference in Gibbs energy (ΔG) of the structures B1 and B2 of the MB N°3 is significantly smaller than for the remaining two MBs, which could mean an easier transition from one conformation to another.

Based on the computer analysis, the MB N°3 was the best candidate for our study. Further, we tested these results experimentally.

5.3.2 The molecular beacons behaviour in water solution

We have further subjected the three selected molecular beacons designs from the previous comparison to an experimental study. To identify the best MB design, we performed a series tests in a water environment keeping the experimental conditions identical for all three MBs. We modified the selected MBs with a fluorescein molecule (5' 6-FAM), covalently attached at the 5' end as a fluorophore, and with a 3' Black Hole Quencher®-1 molecule (3BHQ_1) at the 3' end as a quencher. We then compared them based on thermal stability and the ability to detect target miRNA molecules.

The first experiment aimed to determine the magnitude of the fluorescence value, after the miRNA hybridization using. For each MB design, we made MB concentration series with a large amount of the miRNA (a 5-fold molar excess). The prepared samples were incubated at 37 ° C for 10 min and then the fluorescence value was measured.

Based on the results (see *Figure 5.4*), it can be concluded that with increasing concentration of MB, the fluorescence value also increases almost linearly. This growth is visible for all three MBs. At higher concentrations (12 and 15 μM) the MB N°3 gives the highest fluorescence value, whereas at lower concentrations, the MB N°5 fluorescence is most intense. Based on this experiment, these two designs appear to be better than the MB N°2.

In order to assess, if the hybridization is proceeding quantitatively at 37 °C, we investigated the quantitative rate of hybridization between the MB and the miRNA. We heated the samples to 80 °C to completely open the MB stems, which would facilitate access of the miRNA to the

loop sequence. With slow cooling, the hybridization rate is close to 100 %. We measured the fluorescence value again and compared the obtained data with each other (see *Figure 5.4*, lighter colours).

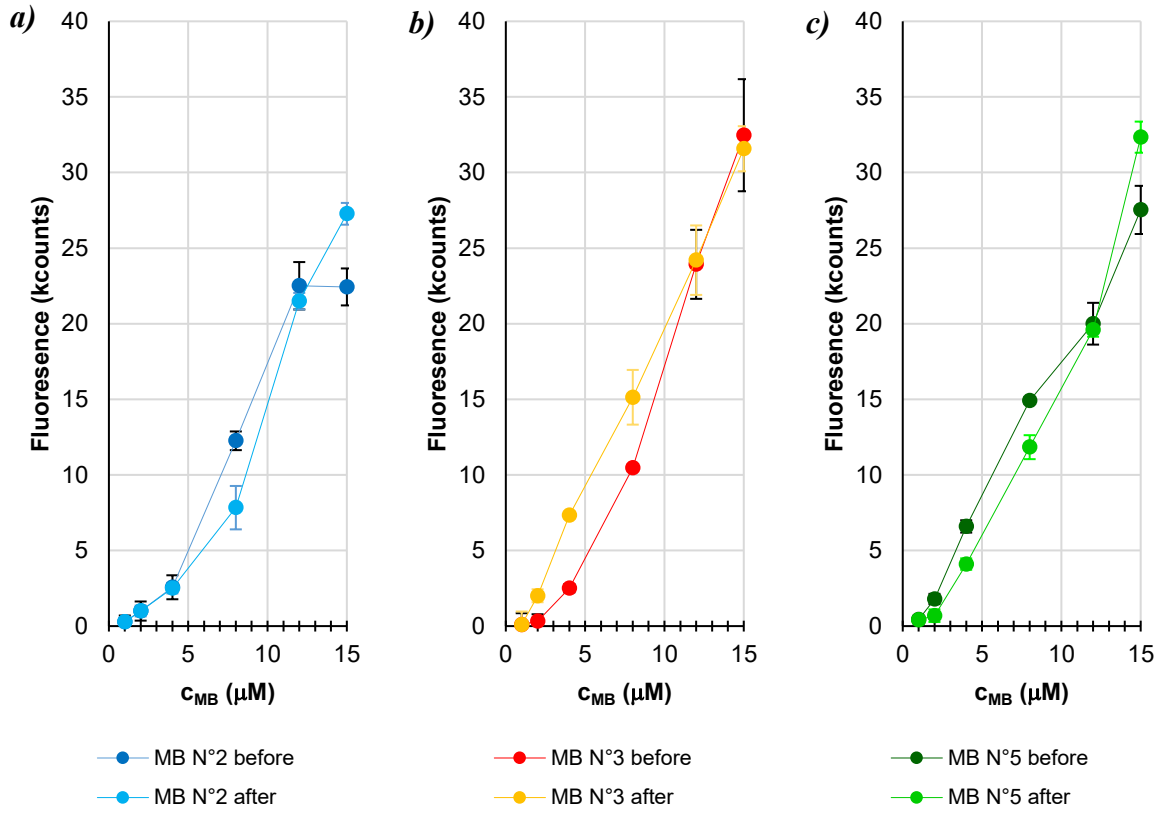

Figure 5.4: The fluorescence intensity as a function of the molecular beacon concentration (c_{MB}) for the ***a)*** MB N°2 ***b)*** MB N°3 and ***c)*** MB N°5 before and after heating, comparing the rate of hybridization of the individual MBs

The hybridization takes place even at 37 °C in all MBs, however, we see the small differences between the individual MBs. For MB N°2 (see *Figure 5.4**a***) there is a small difference at the higher concentrations, while, conversely, for MB N°3 (see *Figure 5.4**b***) a difference can be seen at lower concentrations. MB N°5 (see *Figure 5.4**c***) shows the largest differences at all concentrations, but this difference is not substantial. It can be thus concluded that all three MBs hybridize well enough at 37 °C, making them potential candidates for measurement in living cells.

To determine the sensitivity of the individual MBs for the miRNA detection, we performed the following experiment. We added significantly lower molar amounts of the miRNA to samples with 8 uM concentration of MBs so that the resulting concentrations of miRNAs were 20 nM, 50 nM, 200 nM, 500 nM and 1000 nM. The lowest concentration of the miRNA is up to

400 times lower than the MB concentration, which should be sufficiently small to determine the differences in MB sensitivity. The samples were incubated for 1 h and for 20 h at 37 °C and then the fluorescence was measured (see *Figure 5.5*).

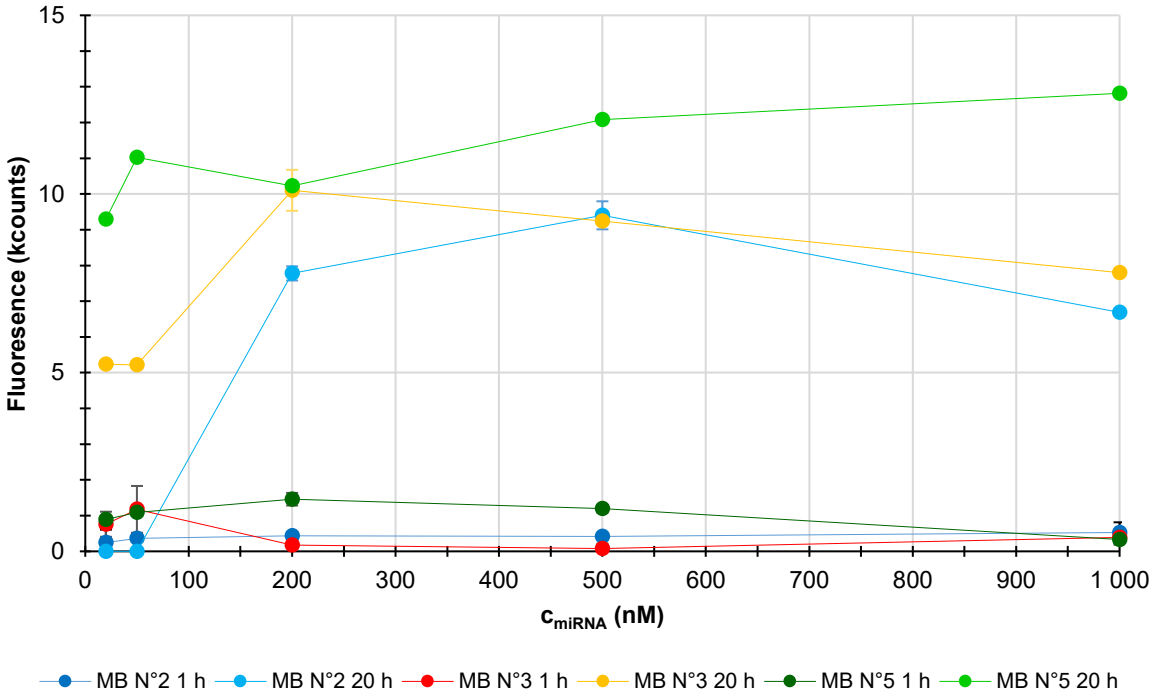

Figure 5.5: The fluorescence intensity as a function of the miRNA concentration (c_{miRNA}) for the three selected MBs incubated for 1 h or 20 h, comparing the detection sensitivities of the individual MBs

Generally, the longer incubation time (20 h) shows significantly higher fluorescence with a several-times increased intensity (10-fold for the MB N°5 at all the miRNA concentrations). Even at a 20 nM and 50 nM miRNA concentration, the MB N°3 and the MB N°5 show a detectable fluorescence after 20 h incubation. The fluorescence value for the MB N°2 at this concentration remained very low even after a longer reaction time. These results suggest that the ideal candidate could be the MB N°5.

The decisive experiment for selecting the most suitable MB, was the study of the hybridization kinetics. The aim was to determine how fast the hybridization with the targeted miRNA molecules takes place at different miRNA concentrations. We used a constant molecular beacon concentration (10 µM) throughout the experiments. For each MB, we monitored three different miRNA concentrations. In the first case, we used the miRNA concentration of 20 µM (twice the concentration of MB, thus designated as 1:2), in the second case 10 µM (designated 1:1) and in the latter case we used only 1 µM (designated 10:1).

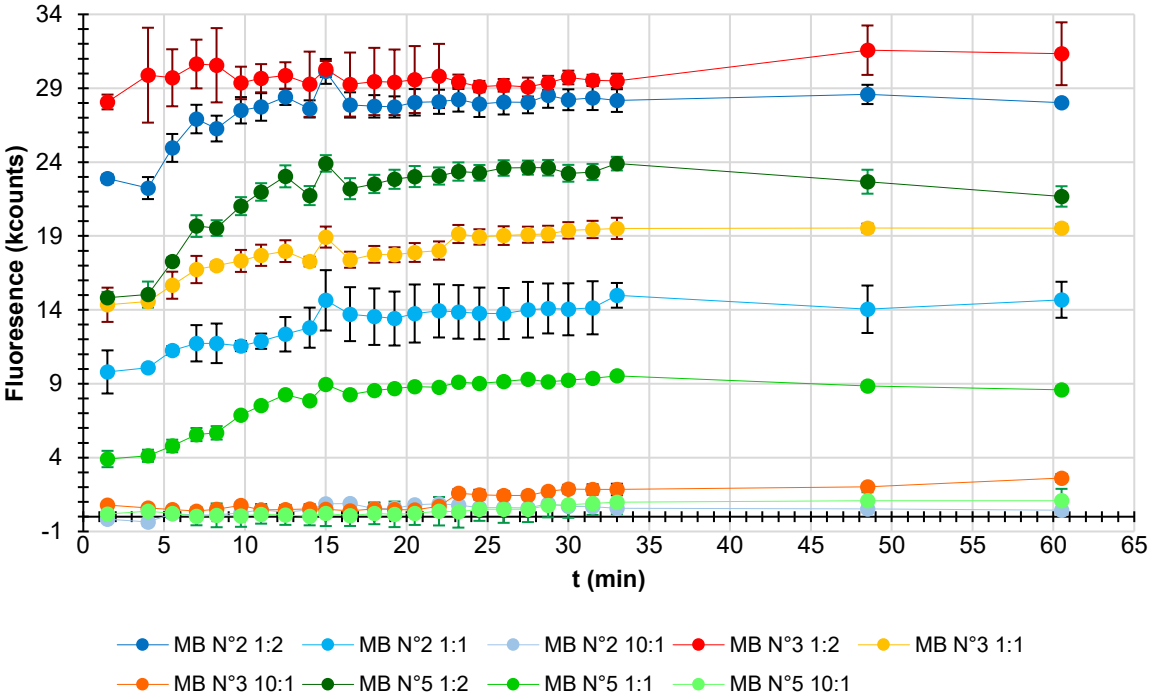

Figure 5.6: The fluorescence intensity as a function time (t) for the three selected MBs with different ratios of MB and miRNA concentrations. The ratios of the individual labels indicate the ratio of the MB and miRNA concentrations

We compared the obtained kinetic profiles of all three MBs at different miRNA concentrations (see *Figure 5.6*). All samples with 1:2 and 1:1 ratios show similar behaviour – approximately 10 min from the start of the reaction, a constant fluorescence value is reached, which later increases only minimally. However, the MB N°3 reaches the highest fluorescence value at all three concentration ratios. Based on these results and the results of theoretical simulations, we chose the MB N°3 design for the further optimization steps, leading to the construction of the entire detection system.

To better understand how fast hybridization occurs, we measured the kinetics for MB N°3 during the first 6.5 min. We used twice the concentration of the miRNA compared to the concentration of the MB (1:2 ratio). Due to the lengthy acquisition time, this measurement was performed in only one replicate.

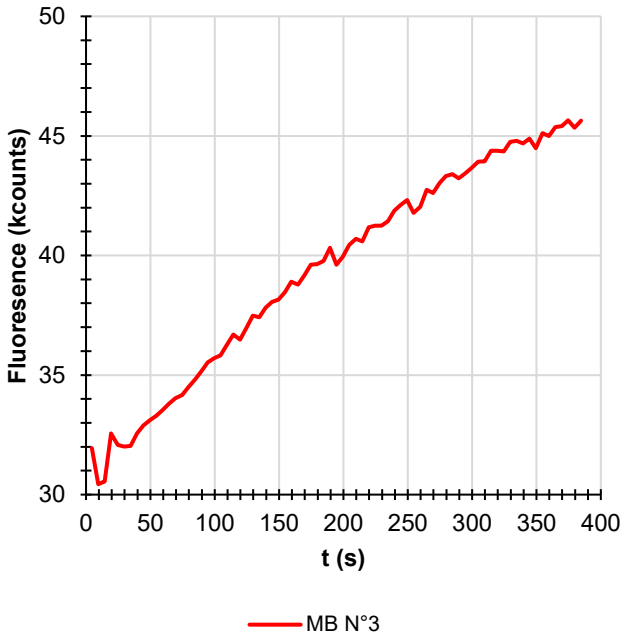

Figure 5.7: The fluorescence intensity as a function time (t) for the MB N°3 showing the hybridization kinetics for the MB N°3 during the first 6.5 min

As can be seen in see *Figure 5.7*, the fluorescence value is already high since in the very beginning, indicating that hybridization occurs immediately after the addition of the miRNAs to the MB solution. Afterwards, the fluorescence value gradually increases and start to stabilize towards the end, which confirms the very fast hybridization kinetics.

5.3.3 End modifications of the selected molecular beacon

After selecting and characterizing the best MB design, we perform its end modifications. Firstly, we attached a gadolinium-containing complex terminated with an azide group to the alkyne group at the 5' end of the MB, by a click reaction. In the second step, we attached a DBCO-PEG_4-NHS ester to the amine group at the 3' end of the MB (amide bond formation).

We monitored the progress of both reactions by the LC-MS chromatography. From the chromatogram, we determined the peak belonging to the product and then displayed its MS spectrum. In the MS spectrum, we identified the most intense peak and from their mass to charge ratio (m/z), we calculated the relative molar mass (see *Table 5.3* and *5.4*), according to the formula:

$$M_w = m/z \cdot x + x, \qquad (2)$$

where x represents how many times the given peak is charged.

Table 5.3: Comparison of the mass to charge ratio (m/z) before and after the reaction between gadolinium-containing complex terminated with the azide group and the alkyne group at the 5' end of the MB, together with the calculated molecular weight (M_w) for this click reaction

Charge	**Before reaction**		**After reaction**	
	m/z	**Calculated M_w**	**m/z**	**Calculated M_w**
10x	1107.27901	11082.79	–	–
7x	1582.40376	11083.83	1683.68713	11792.81
6x	1846.30470	11083.83	1964.65813	11793.95
5x	2215.76446	11083.82	2357.76449	11793.82
4x	2769.97256	11083.89	–	–
Average		**11083.84**		**11793.53**

It can be seen, that the difference in relative molar mass before and after the click is 709.69 (the theoretical relative molar mass difference is 708.75), which means a successful reaction.

The second end modification was reaction with an NH_2 group at the 3' end of the MB with a DBCO-PEG_4-NHS ester to form an amide bond. We used again the LC-MS to assess the progress of the reaction and the data were tabulated (see *Table 5.4*).

Table 5.4: Comparison of the mass to charge ratio (m/z) before and after the reaction between the NH_2 group at the 3' end of the MB with a DBCO-PEG_4-NHS ester, together with the calculated molecular weight (M_w) for that amide bond formation

Charge	**Before reaction**		**After reaction**	
	m/z	**Calculated M_w**	**m/z**	**Calculated M_w**
7x	1683.68713	11792.81	1769.15521	12391.09
6x	1964.65813	11793.95	2064.01976	12390.12
5x	2357.76449	11793.82	2476.94079	12389.70
Average		**11793.53**		**12390.30**

From the calculation, the difference in relative molar mass is 596.78, while the theoretical difference in relative molar mass should be 534.61. We could not explain the difference between the experimental and theoretical relative molar mass in a straightforward way, but this fact had no effect on the MB behaviour (as can be seen in the following subchapters).

To increase the yield from the original 59 % and to eliminate this unexpected difference in the relative molar masses, we used 500mM HEPES solution with pH = 7.4 instead of a 10% solution of the dry triethylamine in the dry DMSO as a buffer system. Unfortunately, this change in buffer reduced the yield to 34 % and the difference, in relative molar masses of 62.15 remained.

Further, we proceeded with the modified MBs to the next steps of the probe development, such as the attachment of the MBs to the FNDs.

5.4 Surface modification of the FNDs leading to the MB attachment

In order to be able to attach the modified molecular beacon to the fluorescent nanodiamonds surface, we first had to modify them appropriately.

5.4.1 Direct azidation of the fluorescent nanodiamonds

In order to attach the DBCO-terminated MB to the FNDs surface, it was necessary to introduce an azide group on the FND surface. To make the detection system as sensitive as possible, the MBs had to be connected as close as possible to the surface of the FNDs. For that reasons, we chose two approaches for a direct crystal lattice modification, using $AgNO_3$ and AgF. In addition to these two direct approaches, we also tried FNDs functionalization with a polymer modified with azide groups.[107]

To be able to determine the amount of azide groups on the fluorescent nanodiamonds surface, we used a procedure based on the detection of a fluorescent complex DBCO-DNA-Atto-488 that would attach specifically to the azide groups of modified fluorescent nanodiamonds. To calibrate this method, we prepared a series of solutions with different concentrations of DBCO-DNA-Atto-488. We then detect the DBCO-DNA-Atto-488 by measuring its fluorescence (emission from 505 to 600 nm). From the maximum fluorescence value (at 535 nm) for each concentration, we constructed a calibration curve (see *Figure 5.8*). We used fitting with a linear function using the least squares method. The fit result expresses the dependence of the

fluorescence value (F) on the DBCO-DNA-Atto-488 concentration ($c_{DBCO\text{-}DNA\text{-}Atto\text{-}488}$). Using this equation and the obtained values, we can now determine the concentration of azide groups on the surface of fluorescent nanodiamonds based on the measured fluorescence value.

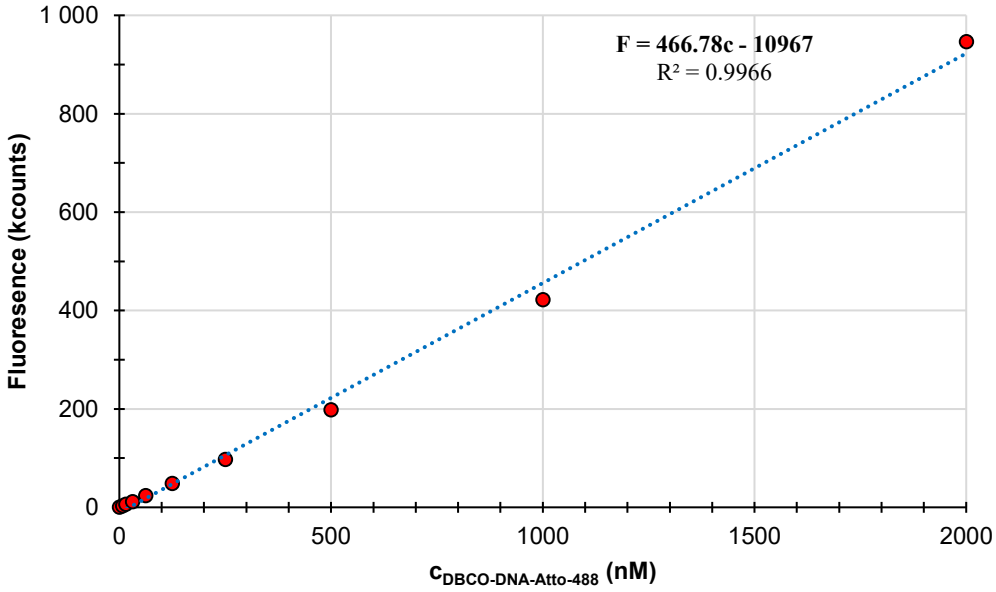

Figure 5.8: The fluorescence intensity as a function of DBCO-DNA-Atto-488 concentration ($c_{DBCO\text{-}DNA\text{-}Atto\text{-}488}$). Red dots represent the measured values and the blue dashed line is the linear fit of the data. The fitting equation is depicted as an inset, where F is fluorescence value, c is DBCO-DNA-Atto-488 concentration and R^2 is a statistical parameter representing the linearity of the measured data. Using this equation, we can then determine the concentration of azide groups on the surface of fluorescent nanodiamonds based on the measured fluorescence value.

After the calibration, we then used this method to characterize the azide-modified fluorescent nanodiamonds prepared by the three methods mentioned above. For the experiments, we used the same excess of DBCO-DNA-Atto-488 as for the calibration.

Table 5.5: Calculated amount of the azide groups on the FNDs surface (c_{N_3}) for three different approaches using the linear fit equation obtained from the previous calibration. F stands for the measured fluorescence value.

Approach	**F (counts)**	**c_{N_3} (nM)**
$AgNO_3$	113 902	267.5
AgF	122 033	284.9

Polymer	30 121	88.0

The determined the concentration of the azide groups on the FNDs surface are summarized in *Table 5.5*. We performed this calculation using the equation resulted from calibration curve. We have found out, that the approaches using direct modification result in higher concentration of the azide groups than the using polymer-based approach. The highest concertation was reached for the AgF modification, consequently, we used these FNDs in the next step.

5.4.2 Azide-DBCO reaction on the FNDs surface

The last optimization step, for preparation of the entire detection system, was the optimization of the reaction between the DBCO-terminated molecular beacon with azidated fluorescent nanodiamonds. Because we tried to attach as many DNA molecules to the surface of fluorescent nanodiamonds as possible due to the higher detection sensitivity. For this optimization, we used (similarly to the *part 5.4.1*) the DBCO-DNA-Atto-488 to observe the reaction conversion for different conditions. We also used the same calibration curve, to calculate the concentration of the attached DNA molecules (see *Figure 5.8*). All approaches were performed in DMSO, except for approach (**5**), which was in water.

To find the best approach, we tried seven different approaches. In the first two approaches (**1** and **2**), after adding the DBCO-DNA-Atto-488 to a colloidal solution of the azidated fluorescent nanodiamonds, we heated the reaction mixture to 45 °C for 3.5 days. The two approaches differed in the amount of the DBCO-DNA-Atto-488, which was 2 μM for the first approach and 4.5 μM for the second. The higher concentration resulted in a slightly increased fluorescence (see *Table 5.5*), suggesting more DBCO-DNA-Atto-488 on the surface of the FNDs, but this increase was only minimal.

Therefore, we tried freeze and thaw approaches. In the following approaches (**3** and **4**), we used 2 μM and 10 μM DBCO-DNA-Atto-488, respectively. In both cases, the samples were frozen at –80 °C for 2 h and then thawed at RT. Afterwards, we repeated the process with the freezing of 16 h. From the fluorescence values and the calculated concentration (see *Table 5.5*), it can be clearly seen, that the freeze and thaw approaches are better than heating to 45 °C.

We then studied the effect of the reaction medium on the course of the reaction. We used water in approach (**5**), while we used DMSO in approach (**6**) and the same freeze and thaw cycles as in the previous two approaches. Approach (**6**) is the same as approach (**4**), but we repeated it

due to a parallel comparison between approaches (**5**) and (**6**). In both cases, we used the same concentration of the DBCO-DNA-Atto-488, 10 μM. It is clear (*see Table 5.5*), that the reaction proceeds better in the DMSO.

In the last (**7**) approach, we combined the freeze and thaw approaches with salt-adding. We used the same conditions as in the approach six, but after completing ten freeze and thaw cycles (with 5 min for freezing each time), we added such the NaI solution in the DMSO, with the resulting salt concentration in the whole solution of 100 mM. We repeated the freeze and thaw cycles three times and increased the salt concentration again to 250 mM. This was repeated once more for a final concentration of the 500 mM (for more information see *part 4.3.4*). The results show (see *Table 5.5*), that the approach seven combining freeze-thaw cycles followed by a gradual addition of salt (NaI) is clearly the best and allows us to attach the most DBCO-DNA molecules to the surface of the FNDs.

Table 5.5: Table of used approaches and the fluorescence values (F) of the FNDs after DBCO-DNA-Atto-488 attachment together with the calculated concentration of DBCO-DNA-Atto-488 (c) on the FNDs surface. All values were measured using same FNDs-N_3 concentration (1 mg/ml).

Approach	F (counts)	c (nM)
1	25 157	77
2	27 626	83
3	83 257	202
4	106 755	252
5	77 525	190
6	100 776	234
7	419 210	916

5.5 Characterization of the prepared detection system

After successful attachment of the MBs terminated with a gadolinium-containing complex to the FNDs surface, we first characterized the whole system.

5.5.1 The number of the MBs attached to the FNDs surface

To determine the number of the MBs attached to the FNDS surface, we used the following information:

(I) Each MB contains one complex containing Gd^{3+} and thus one gadolinium atom.

(II) The gadolinium content was determined by ICP-MS/MS to be 1.43 ppb (**w**).

(III) 20 μg of the FND-MB (**m**) in 5.0 ml of water was used for analysis.

(IV) 1 μg FNDs contains $4.355 \cdot 10^9$ particles (**N'**).

(V) The relative molar mass of gadolinium is 157.25 (**M**).

(VI) 1 mol of FNDs contains $6.022 \cdot 10^{23}$ particles ($\mathbf{N_A}$).

We then used the following formula to calculate the number of gadolinium atoms [N(Gd)] and thus the number of MBs per 1 FND particle:

$$\frac{\mathrm{N(Gd)}}{1\ \mathrm{FND}} = \frac{\mathrm{w} \cdot \mathrm{N_A}}{200 \cdot \mathrm{M}} \cdot \frac{1}{\mathrm{m} \cdot \mathrm{N'}} \cdot 10^{-6} = 314 \qquad (3)$$

where the used values are listed above. The constant 200 results from this dilution.

Based on these calculations, we concluded that we attached on average approximately 314 MBs to the surface of one fluorescent nanodiamond.

5.5.2 The number of the MBs capable for binding the target DNA molecule

To determine how many of the attached MBs to the FNDs surface can actually bind the target molecule, we used a fluorescently labelled complementary DNA molecule (cDNA-Atto-488) instead of the target miRNA molecule, because the interaction between two DNA molecules is generally stronger than between DNA and RNA.

We added this molecule (cDNA-Atto-488) in a molar excess to the colloidal solution of fluorescent nanodiamonds with molecular beacons (FNDs-MBs). After hybridization, we quantitatively removed free cDNA-Atto-488 molecules by centrifugation. Subsequently, we added a 20-fold molar excess of the target DNA molecule (cDNA), which is the same as previous one but it is not labelled. We kept the reaction at 75 °C for 30 min and let it cool to room temperature for another 1 h. During the reaction, the cDNA-Atto-488 is exchanged for cDNA in duplex with MBs. This exchange is statistically controlled because there is a 20-fold

excess of cDNA over cDNA-Atto-488, so we can assume that maximal achievable exchange occurs. Then we centrifuged this sample seven-times and collected the supernatant. We measured the fluorescence of this supernatant and of the pellet (see *Table 5.6*).

The reason why we did measure the fluorescence of the attached cDNA-Atto-488 directly is that DNA molecules can also bind to FNDs-MBs non-specifically (absorption). This non-specific interaction would subsequently cause an incorrect (higher) determination of the number of MBs that are able to bind the target DNA molecule. Therefore, we chose the procedure of displacing fluorescent DNA (cDNA-Atto-488) with its non-fluorescent analogue (cDNA), because this exchange eliminates the effect of non-specific absorption of DNA molecules on the surface of FNDs-MBs.

In order to be able to determine this DNA concentration (cDNA-Atto-488) from the measured fluorescence value, we had to construct a calibration. To calibrate this method, we prepared a series of solutions with different concentrations of cDBCO-DNA-Atto-488. We then detect the cDBCO-DNA-Atto-488 by measuring its fluorescence (emission from 505 to 600 nm). From the maximum fluorescence value (at 535 nm) for each concentration, we constructed a calibration curve (see *Figure 5.9*) that we further used for establishing cDBCO-DNA-Atto-488 concentration on the FNDs surface. We used fitting with a linear function using the least squares method. The fit result expresses the dependence of the fluorescence value (F) on the cDBCO-DNA-Atto-488 concentration ($c_{cDBCO\text{-}DNA\text{-}Atto\text{-}488}$). Using this equation and the obtained values, we can now determine the concentration of cDBCO-DNA-Atto-488 on the surface of fluorescent nanodiamonds based on the measured fluorescence value.

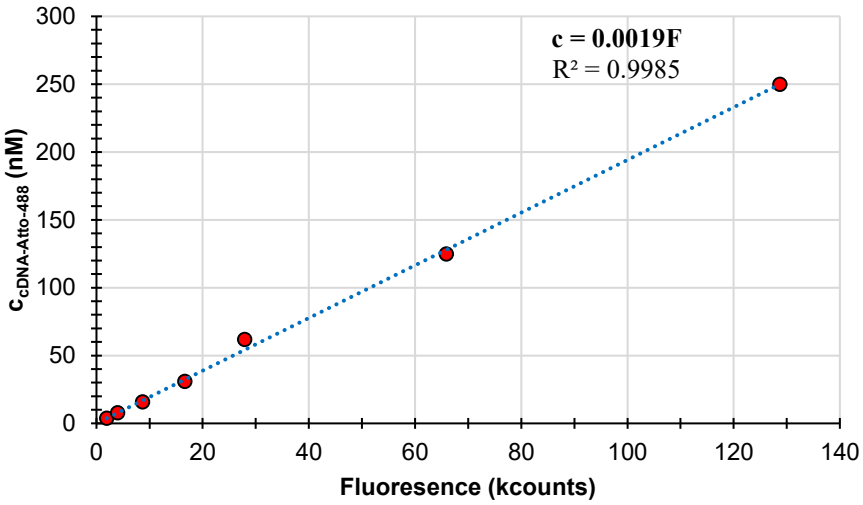

Figure 5.9: The cDBCO-DNA-Atto-488 concentration ($c_{cDBCO\text{-}DNA\text{-}Atto\text{-}488}$) as a function of fluorescence intensity. Red dots represent the measured values and the blue dashed line is the linear fitting function used. The fitting equation is depicted as an inset, where F is fluorescence value, c is cDBCO-DNA-Atto-488 concentration and R^2 is a statistical parameter representing the linearity of the measured data. Using this equation, we can then determine the concentration of cDBCO-DNA-Atto-488 on the surface of fluorescent nanodiamonds and in the supernatant based on the measured fluorescence value.

We then converted this concentration to the number of molecular beacons (N_{MB}). We used the following information to determine the number of the MBs that can bind the target molecule:

(I) After addition of the excess cDNA-Atto-488 molecules under optimal conditions (temperature, reaction time, reaction medium), quantitative hybridization with MBs occurs.

(II) After adding a huge excess (20 molar excess) of the cDNA to FNDs with bound cDNA-Atto-488 and heating to 75 °C, there is maximal exchange of the cDNA-Atto-488 for the cDNA molecules in duplex with the MBs.

(III) After seven centrifugations, any excess DNA molecules present in the supernatant are removed.

(IV) All fluorescence measurements were in a volume of 100 µl (**V**).

(V) $2.53 \cdot 10^{11}$ FNDs are presented in 100 µl of solution (**N**).

(VI) 1 mol of FNDs contains $6.022 \cdot 10^{23}$ particles ($\mathbf{N_A}$).

We then used the following relationship for the calculation:

$$\frac{\mathrm{N(MB)}}{1\ \mathrm{FND}} = \frac{\mathrm{c \cdot V \cdot N_A}}{\mathrm{N}} \cdot 10^{-15} \tag{4}$$

where the used values are listed above, c represents the cDNA-Atto-488 concentration that we calculated using the above-mentioned calibration. The constant 10^{-15} was added as a unit correction.

Table 5.6: Measured fluorescence values (F) and calculated amount of the MBs on the FNDs surface (N_{MB}) capable for binding the target molecule

		F (counts)	**c (nM)**	**N_{MB} / FND**
Before washing	pellet + supernatant	56 101	107	25
After washing	supernatant	46 160	88	21
	FNDs pellet	9 505	18	4

Based on the values calculated in *Table 5.6*, we see that even though we used a 20-fold molar excess of the cDNA, not all cDNA-Atto-488 in the duplex with MBs was completely replaced. An important finding is that the number of MBs bound to 1 FND particle before washing is the same as the sum of the number of MBs present in the supernatant and on the particles after washing. From these results, we see that our detection system is capable for binding up to 25 target DNA (RNA or miRNA) molecules to a single FND particle.

5.5 Quantum sensing using relaxometry

Finally, to verify the functionality of the developed quantum probes, we measured the T_1 relaxation time of the fluorescent nanodiamond NV centres. We performed two sets of relaxometry experiments, before and after additions of the probed cDNAs to the FNDs solution, to determine the effect of cDNA attachment onto the NV T_1 relaxation time. First, we have characterized T_1 relaxation times for the MBs in the absence of the target molecule – i.e. with the MBs in a closed state and the Gd^{3+} ions close to the NV centres.

The samples for the relaxometry measurements were prepared as follows. First, the microscope cover glass was cleaned by plasma and then washed in acetone, ethanol, and water. A cellwell was attached onto the dried cover glass and a 20 µl of 0.01% poly(L-lysine) was added in one

of the wells for better particle adhesion. After 30 min, the cellwell was washed 5 – 8 times and after drying, 4 µl of 0.05 mg/ml FND-MBs solution was placed inside the well. To avoid evaporation, the well was sealed with a microscope glass slide, which was cleaned by plasma and by washing in acetone, ethanol and water. A total number of ~ 40 single isolated fluorescence spots (measurements of randomly selected single particles) were selected for the T_1 measurement. The resulting T_1 relaxation time histogram of the individual particles is shown in *Figure 5.10* ***a)***. The black curve was created by a polynomial fitting of the histogram values. This sample exhibited relatively short averaged T_1 time of 28 µs, as expected.

We have then added 20-fold molar excess of target DNA molecule (cDNA) to colloidal solution of fluorescent nanodiamonds with covalently binding closed MBs on their surface. Subsequently, we quantitatively removed excess cDNA molecules by centrifugation. In this reaction, the target DNA molecules bind to MBs on the surface of the FNDs, the MBs opens up and the Gd^{3+} molecules move further away from the NV centres, which should result in the prolongation of the T_1 relaxation time. The T_1 measurement, as well as the subsequent evaluation, was the same as in the previous sample. The measured histogram of the second sample is shown in *Figure 5.10* ***b)***. As can be seen from the distribution, the T_1 relaxation times has prolonged to the 39 µs on average. This is in line with the sensing mechanism, as in the presence of the target miRNA molecules, MBs are in open conformation and the Gd^{3+} ions are further away from the NV centres.

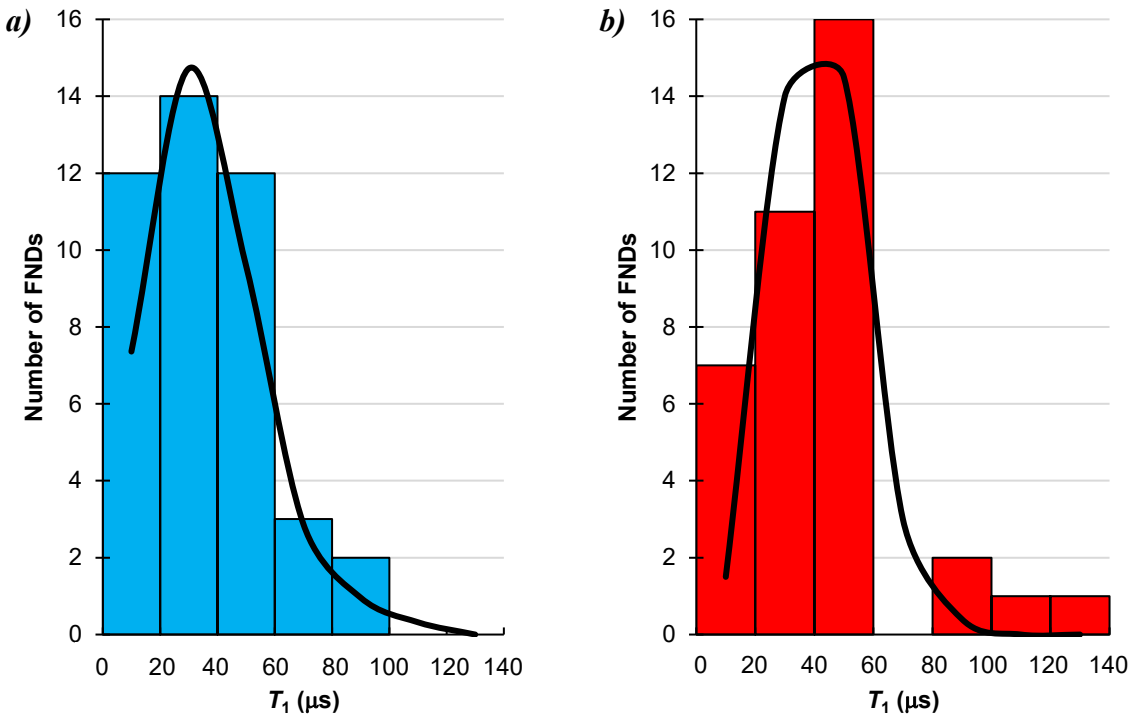

Figure 5.10: The histograms showing the occurrence of the T_1 relaxation times measured on randomly selected single FND particles. ***a)*** Results in the absence of the target DNA molecule and ***b)*** after binding of the target DNA molecule. The black curve is the Poisson distribution fit of the data and serves as an eye guidance for comparison of the two datasets.

The mean T_1 relaxation time was extended in the presence of the target molecule by approximately 39 %. Although better statistic and various concentrations of the probed cDNA would be necessary to characterized the probes quantitatively, these measurements confirm in principle the functionality of the designed and prepared quantum nanoprobes.

6. Discussion

To achieve the goal of monitoring nucleic acids, we have designed a sensor consisting of fluorescent nanodiamonds with covalently attached molecular beacons on their surface that carry the paramagnetic Gd^{3+} ions. The uniqueness of the developed detection system is the possibility of nanoresolution detection in real time at room temperature, which is a key condition for our detection system to be used for localized quantum sensing in living cells. The detection of nucleic acids could take place directly in living cells using confocal microscopy, which allows diffraction-limited resolution. This would allow localized detection of the probed miRNA molecules in a given tissue, thus ensuring early detection of disease processes.

Another very important parameter that needs to be considered is the biocompatibility of our detection system in the biological media. It is essential to ensure that the FNDs with covalently bound MBs on their surface are highly colloidally stable in biologically relevant solutions and that any undesired non-specific adsorption or aggregation does not occur. Biological medium stability tests are one of the things we plan to carry out in the near future by measuring the particle size in differently concentrated phosphate-buffered saline (PBS buffer) and cell medium at different time intervals. However, we assume that the bound MBs (actually oligonucleotides) on the surface should ensure sufficient colloidal stability of our sensor.

The number of MBs on the surface of fluorescent nanodiamonds that can bind target miRNA molecules was determined to be 25 MBs per one FND, which was confirmed by subsequent FND probes characterization as sufficient to detect the target nucleic acid. Such amount of MBs is also sufficient to create a measurable change in T_1 relaxation time after the miRNA bounding, which is supported by the results of the relaxation experiments. We clearly observed an increase in T_1 relaxation time by 39 % after bounding the target nucleic acid. At present, it seems unlikely (and unfavourable, see further) that we would be able to increase the number of MBs bound to the surface of FNDs due to their mutual steric hindrance.

Although the functionality of our detection system has been confirmed by the T_1 relaxation time prolongation upon binding of the target nucleic acid, both measured times (28 and 39 μs) are significantly shorter than the T_1 relaxation time for bare FNDs, which is approximately 100 μs or higher. This difference is probably due to the presence of large amount of Gd^{3+} ions close to the FND surface. Out of the total amount of approximately 314 MBs bounded to a single particle, only ~ 25 were available for detection of nucleic acids, presumably due to the steric

hindrance. As a result, after binding of the target nucleic acids, only small percentage of the Gd^{3+} ions reach a greater distance from the NV centres and the effect of the remaining ones on the T_1 is still significant. In the future, it is possible to optimize our sensor in several ways that would lead to an extension of the T_1 relaxation in the open MB conformation. One is the use of a different paramagnetic label that has a lower effect on the T_1 relaxation time. Another possibility is to bind a lower number of MBs to the surface of FNDs, which means a reduction in the concentration of paramagnetic ions around NV centres. Alternatively, the use of a strategy in which MBs are not bound directly to the surface of the FNDs, but are bound by some chemical linker, bringing them to a greater distance from the surface could be also considered.

In the future, we want to focus on studying the sensitivity of our proposed detection sensor using miRNA molecules that differ from the target miRNA molecule by only one nucleotide exchange. This study is necessary to assess the overall selectivity of our sensor. Furthermore, a huge advantage of the detection system, which we propose, is the easy adaptation to target other miRNA molecules. This can be done by simply changing the sequence of the used MB while the entire sensor architecture as well as the chemical modifications (reactions) remain the same.

Regardless of the modification of our sensor, it is necessary to characterize the prepared sensor in detail in the future work. We plan to implement characterizations using the following measurements. First, it is necessary to make determinations of T_1 relaxation times at different concentrations to calibrate the probe and to determine its sensitivity. This could be done by keeping a constant concentration of FNDs-MBs and adding a different concentrations of the target nucleic acid to create a T_1 time concentration dependence. Furthermore, a time-dependent T_1 measurement should be performed after adding the miRNAs at different time intervals. This is possible with a one-minute resolution.[61,108] All of the above-mentioned measurements must be made on a sufficient number of particles (at least 100 ideally) to obtain statistically relevant results as the amount of NV centres, NV spin properties and the particle size varies greatly for each FND.

The detection system developed in this work opens up a new and unique opportunity for the direct and localized detection of nucleic acids at very low concentrations in living cells and it can thus contribute to the early estimation of disease processes long before clinical signs appear.

7. Conclusion

In our work, we designed a unique quantum sensor for the detection of nucleic acids, which is based on the highly sensitive fluorescent nanodiamonds. The sensing mechanism relies on effect of the paramagnetic species on NV centres electronic spin properties, namely the shortening of NV T_1 relaxation time. For the detection of the specific miRNA molecules we have functionalized the FND surface with Gd^{3+} modified MBs. The whole developed system was characterized and the functionality of the quantum probes to detected target miRNA was demonstrated using relaxometry measurements. All goals of the thesis have been fulfilled and are summarized below. We have:

(i) designed the molecular beacon composition with optimal behaviour and suitable terminal groups for the quantum sensing with FNDs.

(ii) covalently attached complex containing Gd^{3+} ion to the 5' end of the molecular beacon and DBCO terminal group to the 3' end.

(iii) found the optimal method for the preparation of azidated fluorescent nanodiamonds for the MB attachment.

(iv) found the optimal approach to bind DBCO modified molecular beacons to azidated fluorescent nanodiamonds.

(v) prepared the fluorescent nanodiamonds with covalently attached molecular beacons on their surface and characterized the amount of available MBs for sensing.

(vi) confirmed the functionality of our proposed and prepared detection system by measuring the T_1 relaxation time of fluorescent nanodiamond NV centres in the presence and absence of the target nucleic acid molecule.

The functionality of the developed detection system has been successfully confirmed, however further work is desired for potential application in live-cell detection. The selectivity of the detection system to single-nucleotide mismatched nucleic acids have to be monitored to confirm the specify of the system. The colloidal stability over time of the detection system in the biological media needs to be confirmed. The sensitivity of our sensor after adding different amounts of target nucleic acids needs to be determined. The obtained dependence of T_1 relaxation time on miRNA concentration will be the subsequently used to determine the

unknown miRNA concentration from the measured value of T_1 relaxation time. Modifications of the sensing system (such as use of lower amount of MBs or different paramagnetic molecules) should be consider to increase the T_1 relaxation time difference between after hybridization and consequently improving sensitivity. The time-dependent T_1 relaxation time measurements after the introduction of probed nucleic acid should be carried out to estimate the rate of the bounding reaction.

8. References

(1) Lee, R. C.; Feinbaum, R. L.; Ambros, V. The C. Elegans Heterochronic Gene Lin-4 Encodes Small RNAs with Antisense Complementarity to Lin-14. *Cell* **1993**, *75* (5), 843–854. https://doi.org/10.1016/0092-8674(93)90529-y.

(2) Wightman, B.; Ha, I.; Ruvkun, G. Posttranscriptional Regulation of the Heterochronic Gene Lin-14 by Lin-4 Mediates Temporal Pattern Formation in C. Elegans. *Cell* **1993**, *75* (5), 855–862. https://doi.org/10.1016/0092-8674(93)90530-4.

(3) Pasquinelli, A. E.; Reinhart, B. J.; Slack, F.; Martindale, M. Q.; Kuroda, M. I.; Maller, B.; Hayward, D. C.; Ball, E. E.; Degnan, B.; Müller, P.; Spring, J.; Srinivasan, A.; Fishman, M.; Finnerty, J.; Corbo, J.; Levine, M.; Leahy, P.; Davidson, E.; Ruvkun, G. Conservation of the Sequence and Temporal Expression of Let-7 Heterochronic Regulatory RNA. *Nature* **2000**, *408* (6808), 86–89. https://doi.org/10.1038/35040556.

(4) Reinhart, B. J.; Slack, F. J.; Basson, M.; Pasquinelli, A. E.; Bettinger, J. C.; Rougvie, A. E.; Horvitz, H. R.; Ruvkun, G. The 21-Nucleotide Let-7 RNA Regulates Developmental Timing in Caenorhabditis Elegans. *Nature* **2000**, *403* (6772), 901–906. https://doi.org/10.1038/35002607.

(5) Griffiths-Jones, S.; Saini, H. K.; van Dongen, S.; Enright, A. J. MiRBase: Tools for MicroRNA Genomics. *Nucleic Acids Res* **2008**, *36* (Database issue), D154-158. https://doi.org/10.1093/nar/gkm952.

(6) Chang, J.; Nicolas, E.; Marks, D.; Sander, C.; Lerro, A.; Buendia, M. A.; Xu, C.; Mason, W. S.; Moloshok, T.; Bort, R.; Zaret, K. S.; Taylor, J. M. MiR-122, a Mammalian Liver-Specific MicroRNA, Is Processed from Hcr MRNA and May Downregulate the High Affinity Cationic Amino Acid Transporter CAT-1. *RNA Biol* **2004**, *1* (2), 106–113. https://doi.org/10.4161/rna.1.2.1066.

(7) Mishima, T.; Mizuguchi, Y.; Kawahigashi, Y.; Takizawa, T.; Takizawa, T. RT-PCR-Based Analysis of MicroRNA (MiR-1 and -124) Expression in Mouse CNS. *Brain Res* **2007**, *1131* (1), 37–43. https://doi.org/10.1016/j.brainres.2006.11.035.

(8) Weber, J. A.; Baxter, D. H.; Zhang, S.; Huang, D. Y.; Huang, K. H.; Lee, M. J.; Galas, D. J.; Wang, K. The MicroRNA Spectrum in 12 Body Fluids. *Clin Chem* **2010**, *56* (11), 1733–1741. https://doi.org/10.1373/clinchem.2010.147405.

(9) Lu, J.; Getz, G.; Miska, E. A.; Alvarez-Saavedra, E.; Lamb, J.; Peck, D.; Sweet-Cordero, A.; Ebert, B. L.; Mak, R. H.; Ferrando, A. A.; Downing, J. R.; Jacks, T.; Horvitz, H. R.; Golub, T. R. MicroRNA Expression Profiles Classify Human Cancers. *Nature* **2005**, *435* (7043), 834–838. https://doi.org/10.1038/nature03702.

(10) Peter, M. E. Let-7 and MiR-200 MicroRNAs: Guardians against Pluripotency and Cancer Progression. *Cell Cycle* **2009**, *8* (6), 843–852. https://doi.org/10.4161/cc.8.6.7907.

(11) Takamizawa, J.; Konishi, H.; Yanagisawa, K.; Tomida, S.; Osada, H.; Endoh, H.; Harano, T.; Yatabe, Y.; Nagino, M.; Nimura, Y.; Mitsudomi, T.; Takahashi, T. Reduced Expression of the Let-7 MicroRNAs in Human Lung Cancers in Association with Shortened Postoperative Survival. *Cancer Res* **2004**, *64* (11), 3753–3756. https://doi.org/10.1158/0008-5472.CAN-04-0637.

(12) Meng, F.; Henson, R.; Wehbe-Janek, H.; Ghoshal, K.; Jacob, S. T.; Patel, T. MicroRNA-21 Regulates Expression of the PTEN Tumor Suppressor Gene in Human Hepatocellular Cancer. *Gastroenterology* **2007**, *133* (2), 647–658. https://doi.org/10.1053/j.gastro.2007.05.022.

(13) Asangani, I. A.; Rasheed, S. A. K.; Nikolova, D. A.; Leupold, J. H.; Colburn, N. H.; Post, S.; Allgayer, H. MicroRNA-21 (MiR-21) Post-Transcriptionally Downregulates Tumor Suppressor Pdcd4 and Stimulates Invasion, Intravasation and Metastasis in Colorectal Cancer. *Oncogene* **2008**, *27* (15), 2128–2136. https://doi.org/10.1038/sj.onc.1210856.

(14) Schetter, A. J.; Leung, S. Y.; Sohn, J. J.; Zanetti, K. A.; Bowman, E. D.; Yanaihara, N.; Yuen, S. T.; Chan, T. L.; Kwong, D. L. W.; Au, G. K. H.; Liu, C.-G.; Calin, G. A.; Croce, C. M.; Harris, C. C. MicroRNA Expression Profiles Associated with Prognosis and Therapeutic Outcome in Colon Adenocarcinoma. *JAMA* **2008**, *299* (4), 425–436. https://doi.org/10.1001/jama.299.4.425.

(15) Ma, L.; Teruya-Feldstein, J.; Weinberg, R. A. Tumour Invasion and Metastasis Initiated by MicroRNA-10b in Breast Cancer. *Nature* **2007**, *449* (7163), 682–688. https://doi.org/10.1038/nature06174.

(16) Bentwich, I. Prediction and Validation of MicroRNAs and Their Targets. *FEBS Lett* **2005**, *579* (26), 5904–5910. https://doi.org/10.1016/j.febslet.2005.09.040.

(17) Kozomara, A.; Griffiths-Jones, S. MiRBase: Annotating High Confidence MicroRNAs Using Deep Sequencing Data. *Nucleic Acids Research* **2014**, *42* (D1), D68–D73. https://doi.org/10.1093/nar/gkt1181.

(18) Lee, Y.; Han, J.; Yeom, K.-H.; Jin, H.; Kim, V. N. Drosha in Primary MicroRNA Processing. *Cold Spring Harb Symp Quant Biol* **2006**, *71*, 51–57. https://doi.org/10.1101/sqb.2006.71.041.

(19) Lund, E.; Güttinger, S.; Calado, A.; Dahlberg, J. E.; Kutay, U. Nuclear Export of MicroRNA Precursors. *Science* **2004**, *303* (5654), 95–98. https://doi.org/10.1126/science.1090599.

(20) Lee, Y.; Jeon, K.; Lee, J.-T.; Kim, S.; Kim, V. N. MicroRNA Maturation: Stepwise Processing and Subcellular Localization. *EMBO J* **2002**, *21* (17), 4663–4670. https://doi.org/10.1093/emboj/cdf476.

(21) Hutvágner, G.; Zamore, P. D. A MicroRNA in a Multiple-Turnover RNAi Enzyme Complex. *Science* **2002**, *297* (5589), 2056–2060. https://doi.org/10.1126/science.1073827.

(22) Brennecke, J.; Stark, A.; Russell, R. B.; Cohen, S. M. Principles of MicroRNA-Target Recognition. *PLoS Biol* **2005**, *3* (3), e85. https://doi.org/10.1371/journal.pbio.0030085.

(23) Petersen, M.; Nielsen, C. B.; Nielsen, K. E.; Jensen, G. A.; Bondensgaard, K.; Singh, S. K.; Rajwanshi, V. K.; Koshkin, A. A.; Dahl, B. M.; Wengel, J.; Jacobsen, J. P. The Conformations of Locked Nucleic Acids (LNA). *J Mol Recognit* **2000**, *13* (1), 44–53. https://doi.org/10.1002/(SICI)1099-1352(200001/02)13:1<44::AID-JMR486>3.0.CO;2-6.

(24) Válóczi, A.; Hornyik, C.; Varga, N.; Burgyán, J.; Kauppinen, S.; Havelda, Z. Sensitive and Specific Detection of MicroRNAs by Northern Blot Analysis Using LNA-Modified Oligonucleotide Probes. *Nucleic Acids Res* **2004**, *32* (22), e175. https://doi.org/10.1093/nar/gnh171.

(25) Schmittgen, T. D.; Lee, E. J.; Jiang, J.; Sarkar, A.; Yang, L.; Elton, T. S.; Chen, C. Real-Time PCR Quantification of Precursor and Mature MicroRNA. *Methods* **2008**, *44* (1), 31–38. https://doi.org/10.1016/j.ymeth.2007.09.006.

(26) Roush, S.; Slack, F. J. The Let-7 Family of MicroRNAs. *Trends Cell Biol* **2008**, *18* (10), 505–516. https://doi.org/10.1016/j.tcb.2008.07.007.

(27) Tyagi, S.; Kramer, F. R. Molecular Beacons: Probes That Fluoresce upon Hybridization. *Nature Biotechnology* **1996**, *14* (3), 303–308. https://doi.org/10.1038/nbt0396-303.

(28) Wang, K.; Tang, Z.; Yang, C. J.; Kim, Y.; Fang, X.; Li, W.; Wu, Y.; Medley, C. D.; Cao, Z.; Li, J.; Colon, P.; Lin, H.; Tan, W. Molecular Engineering of DNA: Molecular Beacons. *Angew Chem Int Ed Engl* **2009**, *48* (5), 856–870. https://doi.org/10.1002/anie.200800370.

(29) Li, Y.; Zhou, X.; Ye, D. Molecular Beacons: An Optimal Multifunctional Biological Probe. *Biochem Biophys Res Commun* **2008**, *373* (4), 457–461. https://doi.org/10.1016/j.bbrc.2008.05.038.

(30) Tyagi, S. Imaging Intracellular RNA Distribution and Dynamics in Living Cells. *Nat Methods* **2009**, *6* (5), 331–338. https://doi.org/10.1038/nmeth.1321.

(31) Broude, N. E. Stem-Loop Oligonucleotides: A Robust Tool for Molecular Biology and Biotechnology. *Trends Biotechnol* **2002**, *20* (6), 249–256. https://doi.org/10.1016/s0167-7799(02)01942-x.

(32) Ortiz, E.; Estrada, G.; Lizardi, P. M. PNA Molecular Beacons for Rapid Detection of PCR Amplicons. *Mol Cell Probes* **1998**, *12* (4), 219–226. https://doi.org/10.1006/mcpr.1998.0175.

(33) Zuker, M. Mfold Web Server for Nucleic Acid Folding and Hybridization Prediction. *Nucleic Acids Research* **2003**, *31* (13), 3406–3415. https://doi.org/10.1093/nar/gkg595.

(34) Goel, G.; Kumar, A.; Puniya, A. K.; Chen, W.; Singh, K. Molecular Beacon: A Multitask Probe. *J Appl Microbiol* **2005**, *99* (3), 435–442. https://doi.org/10.1111/j.1365-2672.2005.02663.x.

(35) Tyagi, S.; Bratu, D. P.; Kramer, F. R. Multicolor Molecular Beacons for Allele Discrimination. *Nat Biotechnol* **1998**, *16* (1), 49–53. https://doi.org/10.1038/nbt0198-49.

(36) Tsourkas, A.; Behlke, M. A.; Rose, S. D.; Bao, G. Hybridization Kinetics and Thermodynamics of Molecular Beacons. *Nucleic Acids Res* **2003**, *31* (4), 1319–1330. https://doi.org/10.1093/nar/gkg212.

(37) Marras, S. A. E.; Kramer, F. R.; Tyagi, S. Efficiencies of Fluorescence Resonance Energy Transfer and Contact-Mediated Quenching in Oligonucleotide Probes. *Nucleic Acids Res* **2002**, *30* (21), e122. https://doi.org/10.1093/nar/gnf121.

(38) Drake, T. J.; Tan, W. Molecular Beacon DNA Probes and Their Bioanalytical Applications. *Appl Spectrosc* **2004**, *58* (9), 269A-280A. https://doi.org/10.1366/0003702041959406.

(39) Fang, X.; Li, J. J.; Perlette, J.; Tan, W.; Wang, K. Molecular Beacons: Novel Fluorescent Probes. *Anal Chem* **2000**, *72* (23), 747A-753A. https://doi.org/10.1021/ac003001i.

(40) Bonnet, G.; Tyagi, S.; Libchaber, A.; Kramer, F. R. Thermodynamic Basis of the Enhanced Specificity of Structured DNA Probes. *Proc Natl Acad Sci USA* **1999**, *96* (11), 6171. https://doi.org/10.1073/pnas.96.11.6171.

(41) Becker, A.; Reith, A.; Napiwotzki, J.; Kadenbach, B. A Quantitative Method of Determining Initial Amounts of DNA by Polymerase Chain Reaction Cycle Titration Using Digital Imaging and a Novel DNA Stain. *Analytical Biochemistry* **1996**, *237* (2), 204–207. https://doi.org/10.1006/abio.1996.0230.

(42) Kostrikis, L. G.; Tyagi, S.; Mhlanga, M. M.; Ho, D. D.; Kramer, F. R. Spectral Genotyping of Human Alleles. *Science* **1998**, *279* (5354), 1228. https://doi.org/10.1126/science.279.5354.1228.

(43) Morris, T.; Robertson, B.; Gallagher, M. Rapid Reverse Transcription-PCR Detection of Hepatitis C Virus RNA in Serum by Using the TaqMan Fluorogenic Detection System. *J*

Clin Microbiol **1996**, *34* (12), 2933–2936. https://doi.org/10.1128/JCM.34.12.2933-2936.1996.

(44) Täpp, I.; Malmberg, L.; Rennel, E.; Wik, M.; Syvänen, A. C. Homogeneous Scoring of Single-Nucleotide Polymorphisms: Comparison of the 5'-Nuclease TaqMan Assay and Molecular Beacon Probes. *Biotechniques* **2000**, *28* (4), 732–738. https://doi.org/10.2144/00284rr02.

(45) Whitcombe, D.; Theaker, J.; Guy, S. P.; Brown, T.; Little, S. Detection of PCR Products Using Self-Probing Amplicons and Fluorescence. *Nat Biotechnol* **1999**, *17* (8), 804–807. https://doi.org/10.1038/11751.

(46) Marras, S. A.; Kramer, F. R.; Tyagi, S. Multiplex Detection of Single-Nucleotide Variations Using Molecular Beacons. *Genet Anal* **1999**, *14* (5–6), 151–156. https://doi.org/10.1016/s1050-3862(98)00018-7.

(47) Degen, C. L.; Reinhard, F.; Cappellaro, P. Quantum Sensing. *Rev. Mod. Phys.* **2017**, *89* (3), 035002. https://doi.org/10.1103/RevModPhys.89.035002.

(48) Kallerhoff, M.; Karnebogen, M.; Singer, D.; Dettenbach, A.; Gralher, U.; Ringert, R. H. Microcalorimetric Measurements Carried out on Isolated Tumorous and Nontumorous Tissue Samples from Organs in the Urogenital Tract in Comparison to Histological and Impulse-Cytophotometric Investigations. *Urol Res* **1996**, *24* (2), 83–91. https://doi.org/10.1007/BF00431084.

(49) Zhang, X.; Lin, Y.; Gillies, R. J. Tumor PH and Its Measurement. *J Nucl Med* **2010**, *51* (8), 1167–1170. https://doi.org/10.2967/jnumed.109.068981.

(50) Sigaeva, A.; Ong, Y.; Damle, V. G.; Morita, A.; van der Laan, K. J.; Schirhagl, R. Optical Detection of Intracellular Quantities Using Nanoscale Technologies. *Acc. Chem. Res.* **2019**, *52* (7), 1739–1749. https://doi.org/10.1021/acs.accounts.9b00102.

(51) Bai, T.; Gu, N. Micro/Nanoscale Thermometry for Cellular Thermal Sensing. *Small* **2016**, *12* (34), 4590–4610. https://doi.org/10.1002/smll.201600665.

(52) Kettler, K.; Veltman, K.; van de Meent, D.; van Wezel, A.; Hendriks, A. J. Cellular Uptake of Nanoparticles as Determined by Particle Properties, Experimental Conditions,

and Cell Type. *Environmental Toxicology and Chemistry* **2014**, *33* (3), 481–492. https://doi.org/10.1002/etc.2470.

(53) Tsai, P.-C.; Epperla, C. P.; Huang, J.-S.; Chen, O. Y.; Wu, C.-C.; Chang, H.-C. Measuring Nanoscale Thermostability of Cell Membranes with Single Gold–Diamond Nanohybrids. *Angewandte Chemie International Edition* **2017**, *56* (11), 3025–3030. https://doi.org/10.1002/anie.201700357.

(54) Simpson, D. A.; Morrisroe, E.; McCoey, J. M.; Lombard, A. H.; Mendis, D. C.; Treussart, F.; Hall, L. T.; Petrou, S.; Hollenberg, L. C. L. Non-Neurotoxic Nanodiamond Probes for Intraneuronal Temperature Mapping. *ACS Nano* **2017**, *11* (12), 12077–12086. https://doi.org/10.1021/acsnano.7b04850.

(55) Gota, C.; Okabe, K.; Funatsu, T.; Harada, Y.; Uchiyama, S. Hydrophilic Fluorescent Nanogel Thermometer for Intracellular Thermometry. *J. Am. Chem. Soc.* **2009**, *131* (8), 2766–2767. https://doi.org/10.1021/ja807714j.

(56) Gillies, R. J.; Raghunand, N.; Garcia-Martin, M. L.; Gatenby, R. A. PH Imaging. A Review of PH Measurement Methods and Applications in Cancers. *IEEE Eng Med Biol Mag* **2004**, *23* (5), 57–64. https://doi.org/10.1109/memb.2004.1360409.

(57) Schäferling, M. Nanoparticle-Based Luminescent Probes for Intracellular Sensing and Imaging of PH. *Wiley Interdiscip Rev Nanomed Nanobiotechnol* **2016**, *8* (3), 378–413. https://doi.org/10.1002/wnan.1366.

(58) Han, J.; Burgess, K. Fluorescent Indicators for Intracellular PH. *Chem. Rev.* **2010**, *110* (5), 2709–2728. https://doi.org/10.1021/cr900249z.

(59) Arppe, R.; Näreoja, T.; Nylund, S.; Mattsson, L.; Koho, S.; Rosenholm, J. M.; Soukka, T.; Schäferling, M. Photon Upconversion Sensitized Nanoprobes for Sensing and Imaging of PH. *Nanoscale* **2014**, *6* (12), 6837–6843. https://doi.org/10.1039/C4NR00461B.

(60) Chipaux, M.; van der Laan, K. J.; Hemelaar, S. R.; Hasani, M.; Zheng, T.; Schirhagl, R. Nanodiamonds and Their Applications in Cells. *Small* **2018**, *14* (24), 1704263. https://doi.org/10.1002/smll.201704263.

(61) Rendler, T.; Neburkova, J.; Zemek, O.; Kotek, J.; Zappe, A.; Chu, Z.; Cigler, P.; Wrachtrup, J. Optical Imaging of Localized Chemical Events Using Programmable Diamond Quantum Nanosensors. *Nature Communications* **2017**, *8*, 14701. https://doi.org/10.1038/ncomms14701.

(62) Blank, V.; Popov, M.; Pivovarov, G.; Lvova, N.; Gogolinsky, K.; Reshetov, V. Ultrahard and Superhard Phases of Fullerite C60: Comparison with Diamond on Hardness and Wear. *Diam. Relat. Mater* **1998**, *7* (2), 427–431. https://doi.org/10.1016/S0925-9635(97)00232-X.

(63) Wei, L.; Kuo, P. K.; Thomas, R. L.; Anthony, T. R.; Banholzer, W. F. Thermal Conductivity of Isotopically Modified Single Crystal Diamond. *Phys. Rev. Lett.* **1993**, *70* (24), 3764–3767. https://doi.org/10.1103/PhysRevLett.70.3764.

(64) Turcheniuk, K.; Mochalin, V. N. Biomedical Applications of Nanodiamond (Review). *Nanotechnology* **2017**, *28* (25), 252001. https://doi.org/10.1088/1361-6528/aa6ae4.

(65) Lee, D.-K.; Kim, S. V.; Limansubroto, A. N.; Yen, A.; Soundia, A.; Wang, C.-Y.; Shi, W.; Hong, C.; Tetradis, S.; Kim, Y.; Park, N.-H.; Kang, M. K.; Ho, D. Nanodiamond–Gutta Percha Composite Biomaterials for Root Canal Therapy. *ACS Nano* **2015**, *9* (11), 11490–11501. https://doi.org/10.1021/acsnano.5b05718.

(66) Howard, J. W. The Book of Diamonds (Hershey, J. W.). *J. Chem. Educ.* **1940**, *17* (12), 600. https://doi.org/10.1021/ed017p600.2.

(67) Mochalin, V. N.; Shenderova, O.; Ho, D.; Gogotsi, Y. The Properties and Applications of Nanodiamonds. *Nature Nanotechnology* **2012**, *7* (1), 11–23. https://doi.org/10.1038/nnano.2011.209.

(68) Vereshchagin, A. Properties of Detonation Nanodiamonds. *Alt. state tech. University, BTI-Biysk: Publishing house Alt. state tech. University* **2005**.

(69) Danilenko, V. V. Shock-Wave Sintering of Nanodiamonds. *Physics of the Solid State* **2004**, *46* (4), 711–715. https://doi.org/10.1134/1.1711456.

(70) Mochalin, V. N.; Shenderova, O.; Ho, D.; Gogotsi, Y. The Properties and Applications of Nanodiamonds. *Nat Nanotechnol* **2011**, *7* (1), 11–23. https://doi.org/10.1038/nnano.2011.209.

(71) Bradac, C.; Gaebel, T.; Naidoo, N.; Sellars, M. J.; Twamley, J.; Brown, L. J.; Barnard, A. S.; Plakhotnik, T.; Zvyagin, A. V.; Rabeau, J. R. Observation and Control of Blinking Nitrogen-Vacancy Centres in Discrete Nanodiamonds. *Nature Nanotechnology* **2010**, *5*, 345. https://doi.org/10.1038/nnano.2010.56.

(72) Reineck, P.; Lau, D. W. M.; Wilson, E. R.; Fox, K.; Field, M. R.; Deeleepojananan, C.; Mochalin, V. N.; Gibson, B. C. Effect of Surface Chemistry on the Fluorescence of Detonation Nanodiamonds. *ACS Nano* **2017**, *11* (11), 10924–10934. https://doi.org/10.1021/acsnano.7b04647.

(73) Mochalin, V. N.; Gogotsi, Y. Wet Chemistry Route to Hydrophobic Blue Fluorescent Nanodiamond. *J. Am. Chem. Soc.* **2009**, *131* (13), 4594–4595. https://doi.org/10.1021/ja9004514.

(74) Tisler, J.; Balasubramanian, G.; Naydenov, B.; Kolesov, R.; Grotz, B.; Reuter, R.; Boudou, J.-P.; Curmi, P. A.; Sennour, M.; Thorel, A.; Börsch, M.; Aulenbacher, K.; Erdmann, R.; Hemmer, P. R.; Jelezko, F.; Wrachtrup, J. Fluorescence and Spin Properties of Defects in Single Digit Nanodiamonds. *ACS Nano* **2009**, *3* (7), 1959–1965. https://doi.org/10.1021/nn9003617.

(75) Smith, B. R.; Inglis, D. W.; Sandnes, B.; Rabeau, J. R.; Zvyagin, A. V.; Gruber, D.; Noble, C. J.; Vogel, R.; Ōsawa, E.; Plakhotnik, T. Five-Nanometer Diamond with Luminescent Nitrogen-Vacancy Defect Centers. *Small* **2009**, *5* (14), 1649–1653. https://doi.org/10.1002/smll.200801802.

(76) Schirhagl, R.; Chang, K.; Loretz, M.; Degen, C. L. Nitrogen-Vacancy Centers in Diamond: Nanoscale Sensors for Physics and Biology. *Annu. Rev. Phys. Chem.* **2014**, *65* (1), 83–105. https://doi.org/10.1146/annurev-physchem-040513-103659.

(77) Pichot, V.; Comet, M.; Fousson, E.; Baras, C.; Senger, A.; Le Normand, F.; Spitzer, D. An Efficient Purification Method for Detonation Nanodiamonds. *Diamond and Related Materials* **2008**, *17* (1), 13–22. https://doi.org/10.1016/j.diamond.2007.09.011.

(78) Boudou, J.-P.; Curmi, P. A.; Jelezko, F.; Wrachtrup, J.; Aubert, P.; Sennour, M.; Balasubramanian, G.; Reuter, R.; Thorel, A.; Gaffet, E. High Yield Fabrication of Fluorescent Nanodiamonds. *Nanotechnology* **2009**, *20* (23), 235602. https://doi.org/10.1088/0957-4484/20/23/235602.

(79) Schwander, M.; Partes, K. A Review of Diamond Synthesis by CVD Processes. *Diamond and Related Materials - DIAM RELAT MATER* **2011**, *20*, 1287–1301. https://doi.org/10.1016/j.diamond.2011.08.005.

(80) Tzeng, Y.-K.; Zhang, J. L.; Lu, H.; Ishiwata, H.; Dahl, J.; Carlson, R. M. K.; Yan, H.; Schreiner, P. R.; Vučković, J.; Shen, Z.-X.; Melosh, N.; Chu, S. Vertical-Substrate MPCVD Epitaxial Nanodiamond Growth. *Nano Lett.* **2017**, *17* (3), 1489–1495. https://doi.org/10.1021/acs.nanolett.6b04543.

(81) Butler, J. E.; Sumant, A. V. The CVD of Nanodiamond Materials. *Chemical Vapor Deposition* **2008**, *14* (7-8), 145–160. https://doi.org/10.1002/cvde.200700037.

(82) Aharonovich, I.; Castelletto, S.; Simpson, D. A.; Su, C.-H.; Greentree, A. D.; Prawer, S. Diamond-Based Single-Photon Emitters. *Reports on Progress in Physics* **2011**, *74* (7), 076501. https://doi.org/10.1088/0034-4885/74/7/076501.

(83) Bradac, C.; Gaebel, T.; Naidoo, N.; Rabeau, J. R.; Barnard, Amanda. S. Prediction and Measurement of the Size-Dependent Stability of Fluorescence in Diamond over the Entire Nanoscale. *Nano Lett.* **2009**, *9* (10), 3555–3564. https://doi.org/10.1021/nl9017379.

(84) Schirhagl, R.; Chang, K.; Loretz, M.; Degen, C. L. Nitrogen-Vacancy Centers in Diamond: Nanoscale Sensors for Physics and Biology. *Annu. Rev. Phys. Chem.* **2014**, *65* (1), 83–105. https://doi.org/10.1146/annurev-physchem-040513-103659.

(85) Doherty, M. W.; Manson, N. B.; Delaney, P.; Jelezko, F.; Wrachtrup, J.; Hollenberg, L. C. L. The Nitrogen-Vacancy Colour Centre in Diamond. *Physics Reports* **2013**, *528* (1), 1–45. https://doi.org/10.1016/j.physrep.2013.02.001.

(86) Howie, R. A. G. Davies, Ed. Properties and Growth of Diamond. London (The Institution of Electrical Engineers), 1994. 438 Pp. Xvi +, Price £135.00. ISBN 0 85296

875 2. *Mineralogical Magazine* **1995**, *59* (394), 171–171. https://doi.org/10.1180/minmag.1995.59.394.22.

(87) Jarmola, A.; Acosta, V. M.; Jensen, K.; Chemerisov, S.; Budker, D. Temperature- and Magnetic-Field-Dependent Longitudinal Spin Relaxation in Nitrogen-Vacancy Ensembles in Diamond. *Phys. Rev. Lett.* **2012**, *108* (19), 197601. https://doi.org/10.1103/PhysRevLett.108.197601.

(88) Zvyagin, A. V.; Manson, N. B. Chapter 10 - Optical and Spin Properties of Nitrogen-Vacancy Color Centers in Diamond Crystals, Nanodiamonds, and Proximity to Surfaces. In *Ultananocrystalline Diamond (Second Edition)*; Shenderova, O. A., Gruen, D. M., Eds.; William Andrew Publishing: Oxford, 2012; pp 327–354. https://doi.org/10.1016/B978-1-4377-3465-2.00010-4.

(89) Tetienne, J.-P.; Hingant, T.; Rondin, L.; Cavaillès, A.; Mayer, L.; Dantelle, G.; Gacoin, T.; Wrachtrup, J.; Roch, J.-F.; Jacques, V. Spin Relaxometry of Single Nitrogen-Vacancy Defects in Diamond Nanocrystals for Magnetic Noise Sensing. *Phys. Rev. B* **2013**, *87* (23), 235436. https://doi.org/10.1103/PhysRevB.87.235436.

(90) Netz, R. R.; Andelman, D. Neutral and Charged Polymers at Interfaces. *Physics Reports* **2003**, *380* (1), 1–95. https://doi.org/10.1016/S0370-1573(03)00118-2.

(91) Försterová, M.; Svobodová, I.; Lubal, P.; Táborský, P.; Kotek, J.; Hermann, P.; Lukes, I. Thermodynamic Study of Lanthanide(III) Complexes with Bifunctional Monophosphinic Acid Analogues of H4dota and Comparative Kinetic Study of Yttrium(III) Complexes. *Dalton transactions (Cambridge, England : 2003)* **2007**, No. 5, 535–549. https://doi.org/10.1039/b613404a.

(92) Holz, M. L. Banci, L. Bertini and C. Luchinat. Nuclear and Electron Relaxation. The Magnetic Nucleus-Unpaired Electron Coupling in Solution. VCH, Weinheim, New York, Basel, Cambridge, 1991, Pp. 216, DM 118. ISBN 3-527-28306-4. *Magnetic Resonance in Chemistry* **1993**, *31* (13), S154–S154. https://doi.org/10.1002/mrc.1260311327.

(93) Landstrass, M. I.; Ravi, K. V. Resistivity of Chemical Vapor Deposited Diamond Films. *Appl. Phys. Lett.* **1989**, *55* (10), 975–977. https://doi.org/10.1063/1.101694.

(94) Neu, E.; Arend, C.; Gross, E.; Guldner, F.; Hepp, C.; Steinmetz, D.; Zscherpel, E.; Ghodbane, S.; Sternschulte, H.; Steinmüller-Nethl, D.; Liang, Y.; Krueger, A.; Becher, C. Narrowband Fluorescent Nanodiamonds Produced from Chemical Vapor Deposition Films. *Appl. Phys. Lett.* **2011**, *98* (24), 243107. https://doi.org/10.1063/1.3599608.

(95) Zou, Q.; Wang, M. Z.; Li, Y. G. Analysis of the Nanodiamond Particle Fabricated by Detonation. *null* **2010**, *5* (4), 319–328. https://doi.org/10.1080/17458080903531021.

(96) Turner, S.; Lebedev, O. I.; Shenderova, O.; Vlasov, I. I.; Verbeeck, J.; Van Tendeloo, G. Determination of Size, Morphology, and Nitrogen Impurity Location in Treated Detonation Nanodiamond by Transmission Electron Microscopy. *Advanced Functional Materials* **2009**, *19* (13), 2116–2124. https://doi.org/10.1002/adfm.200801872.

(97) Osswald, S.; Yushin, G.; Mochalin, V.; Kucheyev, S. O.; Gogotsi, Y. Control of Sp2/Sp3 Carbon Ratio and Surface Chemistry of Nanodiamond Powders by Selective Oxidation in Air. *J. Am. Chem. Soc.* **2006**, *128* (35), 11635–11642. https://doi.org/10.1021/ja063303n.

(98) Krueger, A.; Ozawa, M.; Jarre, G.; Liang, Y.; Stegk, J.; Lu, L. Deagglomeration and Functionalisation of Detonation Diamond. *physica status solidi (a)* **2007**, *204* (9), 2881–2887. https://doi.org/10.1002/pssa.200776330.

(99) IDA, S.; TSUBOTA, T.; NAGATA, M.; MATSUMOTO, Y.; UEHARA, M.; HOJO, J. Chemical Reaction of Carbonyl Group on Diamond Surface with LiAlH4. *Journal of The Surface Finishing Society of Japan* **2003**, *54* (11), 764–768. https://doi.org/10.4139/sfj.54.764.

(100) Martín, R.; Álvaro, M.; Herance, J. R.; García, H. Fenton-Treated Functionalized Diamond Nanoparticles as Gene Delivery System. *ACS Nano* **2010**, *4* (1), 65–74. https://doi.org/10.1021/nn901616c.

(101) Miller, J. B. Amines and Thiols on Diamond Surfaces. *Surface Science* **1999**, *439* (1), 21–33. https://doi.org/10.1016/S0039-6028(99)00683-4.

(102) Sotowa, K.-I.; Amamoto, T.; Sobana, A.; Kusakabe, K.; Imato, T. Effect of Treatment Temperature on the Amination of Chlorinated Diamond. *Diamond and Related Materials* **2004**, *13* (1), 145–150. https://doi.org/10.1016/j.diamond.2003.10.029.

(103) Hens, S. C.; Cunningham, G.; Tyler, T.; Moseenkov, S.; Kuznetsov, V.; Shenderova, O. Nanodiamond Bioconjugate Probes and Their Collection by Electrophoresis. *Diamond and Related Materials* **2008**, *17* (11), 1858–1866. https://doi.org/10.1016/j.diamond.2008.03.020.

(104) Liu, Y.; Gu, Z.; Margrave, J. L.; Khabashesku, V. N. Functionalization of Nanoscale Diamond Powder: Fluoro-, Alkyl-, Amino-, and Amino Acid-Nanodiamond Derivatives. *Chem. Mater.* **2004**, *16* (20), 3924–3930. https://doi.org/10.1021/cm048875q.

(105) Nakamura, T.; Ohana, T.; Hagiwara, Y.; Tsubota, T. Photochemical Modification of Diamond Powders with Elemental Sulfur and Their Surface-Attachment Behavior on Gold Surfaces. *Phys. Chem. Chem. Phys.* **2009**, *11* (4), 730–734. https://doi.org/10.1039/B814406K.

(106) Kennedy, Z. C.; Barrett, C. A.; Warner, M. G. Direct Functionalization of an Acid-Terminated Nanodiamond with Azide: Enabling Access to 4-Substituted-1,2,3-Triazole-Functionalized Particles. *Langmuir* **2017**, *33* (11), 2790–2798. https://doi.org/10.1021/acs.langmuir.6b04477.

(107) Zhao, L.; Nakae, Y.; Qin, H.; Ito, T.; Kimura, T.; Kojima, H.; Chan, L.; Komatsu, N. Polyglycerol-Functionalized Nanodiamond as a Platform for Gene Delivery: Derivatization, Characterization, and Hybridization with DNA. *Beilstein J Org Chem* **2014**, *10*, 707–713. https://doi.org/10.3762/bjoc.10.64.

(108) Barton, J.; Gulka, M.; Tarabek, J.; Mindarava, Y.; Wang, Z.; Schimer, J.; Raabova, H.; Bednar, J.; Plenio, M. B.; Jelezko, F.; Nesladek, M.; Cigler, P. Nanoscale Dynamic Readout of a Chemical Redox Process Using Radicals Coupled with Nitrogen-Vacancy Centers in Nanodiamonds. *ACS Nano* **2020**, *14* (10), 12938–12950. https://doi.org/10.1021/acsnano.0c04010.